Int J Fract (2012) 173:105–133
DOI 10.1007/s10704-011-9667-x

ORIGINAL PAPER

A multiscale parametric study of mode I fracture in metal-to-metal low-toughness adhesive joints

Ph. Martiny · F. Lani · A. J. Kinloch · T. Pardoen

Received: 10 June 2011 / Accepted: 13 December 2011 / Published online: 24 January 2012

Abstract The failure of adhesively-bonded joints, consisting of metallic adherends and epoxy-based structural adhesive with a relatively low toughness $\sim$200 J/m^2, has been studied. The failure was via quasi-static mode I, steady-state crack propagation and has been modelled numerically. The model implements a 'top-down approach' to fracture using a dedicated steady-state, finite-element formulation. The damage mechanisms responsible for fracture are condensed onto a row of cohesive zone elements with zero thickness, and the responses of the bulk adhesive and of the adherends are represented by continuum elements spanning the full geometry of the joint. The material parameters employed in the model are first quantitatively identified for the particular epoxy adhesive of interest, and their validity is verified by comparison with experimental results. The model is then used to conduct a detailed study on the effects of (a) large variations in the geometrical configuration of the different types of specimens and (b) the adherend stiffness on the predicted value of the adhesive fracture energy, G_a. These numerical modelling results reveal that the adhesive fracture energy is a strong nonlinear function of the thickness of the adhesive layer, the other variables being of secondary importance in influencing the value of G_a providing the adhesive does not contribute significantly to the bending stiffness of the joint. These results which fully agree with experimental observations are explained in detail by identifying, and quantifying, the different sources of energy dissipation in the bulk adhesive contributing to the value of G_a. These sources are the locked-in elastic energy, crack tip plasticity, reverse plastic loading and plastic shear deformation at the adhesive/adherend interface. Further, the magnitudes of these sources of energy dissipation are correlated to the degree of constraint at the crack tip, which is quantified by considering the opening angle of the cohesive zone at the crack tip.

Keywords Adhesive fracture energy · Finite elements · Cohesive zone · Fracture mechanisms · Steady-state crack propagation

Ph. Martiny (✉) · F. Lani
Cenaero, Centre de Recherche en Aéronautique,
Rue des frères Wright 29, 6041 Gosselies, Belgium
e-mail: philippe.martiny@cenaero.be

A. J. Kinloch
Mechanical Engineering Department, Imperial College
London, Exhibition Road, London SW7 2AZ, UK
e-mail: a.kinloch@imperial.ac.uk

F. Lani · T. Pardoen (✉)
Institute of Mechanics, Materials and Civil Engineering,
Université catholique de Louvain, Place Sainte Barbe 2,
1348 Louvain-la-Neuve, Belgium
e-mail: thomas.pardoen@uclouvain.be

F. Lani
e-mail: frederic.lani@uclouvain.be

1 Introduction

Adhesive bonding as a method of joining materials has been drawing more and more interest from many

diverse industries over the last few decades. This interest stems from the many advantages it offers over more traditional joining techniques such as bolting, riveting or welding (Kinloch 1987). Amongst these numerous advantages are (a) a more uniform stress distribution across the joint and, hence, an increased fatigue life, and (b) the ability to join readily dissimilar materials such as metals, plastic, rubbers, composites and glass. Nevertheless, adhesive bonding is still relatively little used in structural applications, where the joint is a safety-critical feature of the design of the component or structure. One of the main reasons for this is that the failure of adhesive joints is difficult to predict and, hence, to properly take into account during the design phase. This problem arises since the failure of adhesive joints involves complex, nonlinear phenomena which generally depend upon a large variety of parameters such as, for example, the type of joint design and the exact geometrical configuration of the joint. As might be expected, experimental studies have been carried out with a view to ascertain these effects. In particular, several researchers (Bascom et al. 1975; Chai 1986, 1988; Kinloch and Shaw 1981) have shown that the adhesive fracture energy, G_a, is a nonlinear function of the thickness of the adhesive layer. This effect was qualitatively explained by Kinloch and Shaw (1981) from the magnitude of the plastic dissipation in the adhesive layer being dependent upon the degree of constraint, which was supported by some experimental evidence (Hunston et al. 1989). Other authors (e.g. Blackman et al. 2003c; Cooper et al. 2009; Kawashita et al. 2008) have further demonstrated that the value of G_a is not significantly dependent on parameters such as the type of adherend material, the thickness of the adherend arms or the type of test specimen geometry (e.g. tapered double-cantilever beam test specimen versus peel test specimen). These observations were attributed to the adhesive fracture energy, G_a, essentially being a 'characteristic material property' at any given thickness of the adhesive layer. However, this hypothesis, which has very important implications for the design of adhesive joints, has not been definitively proven and is still the subject of much debate.

The main goal of the present paper is to undertake a detailed theoretical description of the dependence of the adhesive fracture energy, G_a, upon the specimen type and its geometrical configuration, for a given epoxy-based structural adhesive which has a relatively low toughness and which has been observed to exhibit the typical behaviour as described above. To achieve this overall aim, a numerical model is first developed and validated by comparison with the reported experimental data. The model is then used to predict the dependence of the adhesive fracture energy, G_a, on (a) the geometrical configuration of the different types of specimens and (b) the adherend stiffness. These numerical results are then analysed through detailed inspection of the stress, strain and energy fields and rationales are proposed for the trends that are numerically predicted. These rationales, although applicable for quantitative purposes only to the present low-toughness adhesive, are considered to serve as a solid basis to further our understanding of the behaviour of other epoxy-based structural adhesives which have been shown experimentally to exhibit similar trends.

The idea behind the model that will be developed was first suggested by Needleman (1987) in the context of inclusion debonding in heterogeneous materials, and has been applied recently to cohesive failure in adhesive joints (Blackman et al. 2003b; Cooper et al. 2009; Martiny et al. 2008; Pardoen et al. 2005; Salomonsson and Andersson 2008; Tvergaard and Hutchinson 1994). It consists in following a 'top-down approach' to fracture (Hutchinson and Evans 2000): that is (see Fig. 1), both cohesive zone elements and continuum elements are used to represent the different phenomena taking place at different length scales in the adhesive as it fractures. In addition, the model that will be used computes, in a single calculation, the test-specimen configuration corresponding to the conditions of steady-state crack propagation. These modelling choices are particularly well suited to performing the parametric study envisaged in the present study. Firstly, the model relies on a single set of material parameters, like other types of model in the literature (e.g. Chai and Chiang 1998; Hadavinia et al. 2006), to reproduce accurately the failure of the adhesive for different types of test specimen and over a wide range of geometrical configurations (Martiny et al. 2008). This is in contrast to numerous solutions that can be found in the literature (e.g. Ferracin et al. 2003; Yang et al. 1999, 2000) that rely on material parameters that need to be re-identified experimentally or re-calculated numerically when, for example, the thickness of the adhesive layer is changed (Kafkalidis et al. 2000). Secondly, the proposed model gives a detailed description of the stress state in the adhesive, which is very useful for identifying a rationale for the trends that have been observed

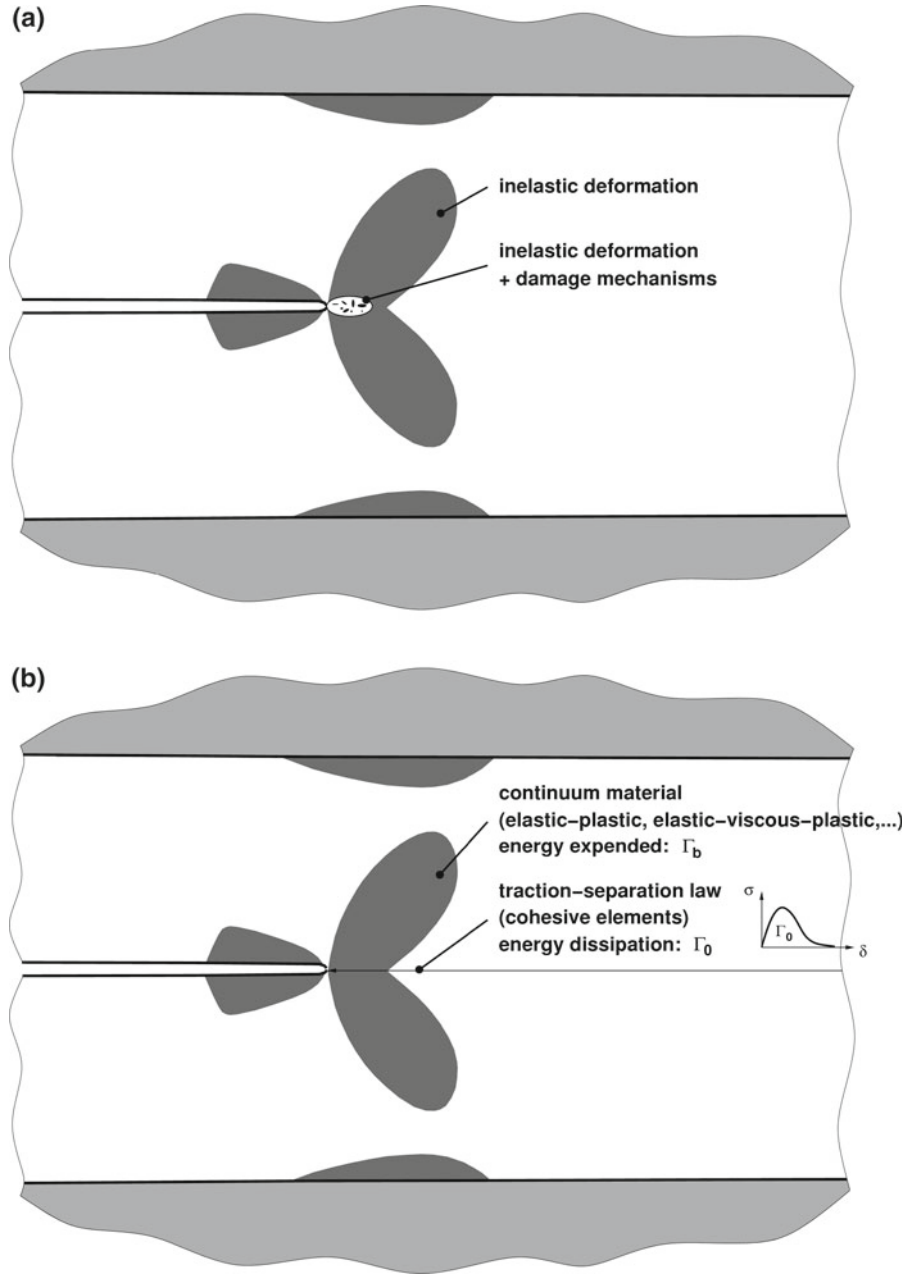

Fig. 1 A schematic representation of **a** the phenomena associated with the fracture of an adhesive layer, and **b** the corresponding model (*dark shaded areas* represent inelastic deformation in the adhesive layer)

experimentally. Again, this is in contrast to some simplified models (e.g. Ferracin et al. 2003; Yang et al. 1999, 2000) which miss these details by replacing the actual adhesive layer by a single cohesive zone. Finally, the proposed model finds the steady-state solution to the problem in a single calculation and, hence, is computationally efficient. This is very desirable when many geometrical configurations of different types of specimen need to be studied, as it is the case in the present study. Yet again, in contrast, transient-solution schemes (e.g. Cui et al. 2003; Hadavinia et al. 2006) only reach the steady-state solution after solving numerous intermediate time-steps, which are required in order to propagate the crack over a distance equal to several adhesive layers thicknesses before reaching the steady-state. This is a very time consuming process, since very small element sizes have to be used to represent the response of the fracture process zone.

A somewhat similar model has been previously used to conduct parametric studies on the toughness of rate-independent materials (Tvergaard and Hutchinson 1992), rate-dependent materials (Landis et al. 2000) and thin ductile layers joining semi-infinite elastic media (Tvergaard and Hutchinson 1994). Also, the present model shares some common features with the one reported by Salomonsson and Andersson (2008), but in their work they set out to identify the cohesive zone model that would best represent the full adhesive layer. The present study aims to add significantly to the understanding gained in these previous studies by considering the toughness of adhesive joints, i.e. by conducting a parametric study on the toughness of a polymeric layer (the adhesive), sandwiched between two elastic-plastic materials with finite dimensions (the adherends). Indeed, it completes the work that was initiated by Pardoen et al. (2005) by studying in depth, and explaining, the different local dissipation mechanisms that contribute to the value of the adhesive fracture energy via an analysis of the detailed stress and strain fields. The model used in the present work will assume that the energy associated with the fracture process zone, as described by the traction-separation law is a constant, and so independent of the stress state. This is indeed a major assumption that will be justified from the experimental validation undertaken, as well as being based on physical arguments related to the mechanisms of damage and failure that occur; and which follow from the relatively low toughness of the adhesive employed in the present work.

The outline of the paper is as follows. Section 2 briefly describes the experimental data that will enable (a) the determination of the material parameters of the model, and (b) the validation of the numerical model and of the values of these material parameters. In Sect. 3 the development of the fundamental model is explained and details are given about its implementation. Section 4 is the core of the paper. It presents and explains the different numerical modelling results. After further calibration and validation of the model, the different potential sources of energy dissipation contributing to the adhesive fracture energy, G_a, are clearly identified and quantified. The effects of the type of test specimen, the geometrical configuration and the stiffness of the adherend on the value of the adhesive fracture energy, G_a, are then systematically considered. Finally, concluding comments are given in Sect. 5.

2 Experimental

2.1 The materials

The adhesive was a hot-cured single-part structural adhesive, namely 'Betamate 73455' manufactured by Dow Automotive, USA. It is an epoxy-paste adhesive, containing a large fraction of silica particles. It possesses a relatively high modulus and low toughness compared with the rubber-toughened epoxy adhesive that was studied recently by the present authors (Martiny et al. 2008). The fracture behaviour of this adhesive was studied experimentally employing both a LEFM tapered double-cantilever beam (TDCB) and an elastic-plastic fracture-mechanics (EPFM) wedge-peel type test specimen. The adhesive and the adherends were also tested in uniaxial tension to determine the stress versus strain behaviour, which is needed for the modelling studies.

2.2 EPFM wedge-peel tests

The adhesive has been previously tested using the wedge-peel test specimen, see Fig. 2a, by Pardoen et al. (2005). A series of test configurations, with various adhesive layer thicknesses, h_{adh}, were manufactured by bonding together 30 mm wide strips cut from a 0.78 mm thick plate of mild steel, after degreasing the surfaces. The thickness of the adhesive layer was controlled by dispersing glass beads or metallic wires with the appropriate diameter within the layer, prior to assembling the joints. The specimens were cured for 45 min at 180°C. The specimens were peeled apart in a testing machine by driving a wedge of thickness, D_w, equal to 1.8 mm between the adherends at a crosshead speed of 10 mm/min, as shown schematically in Fig. 2a. The residual radii of curvature, R_1, and R_2, of both arms were obtained after the test by fitting a circle through a set of points taken, using a profile projector, on the free surfaces of the peeled arms. For each specimen, the values of R_1, and R_2 were averaged to give a single value, R_a, according to:[1]

$$\frac{1}{R_a} = \left[\frac{1}{2}\left(\frac{1}{R_1^{n+1}} + \frac{1}{R_2^{n+1}}\right)\right]^{\frac{1}{n+1}} \tag{1}$$

where n is the strain-hardening exponent of the substrate material. The results that were obtained are given

[1] Note that this formula was mistyped in Pardoen et al. (2005).

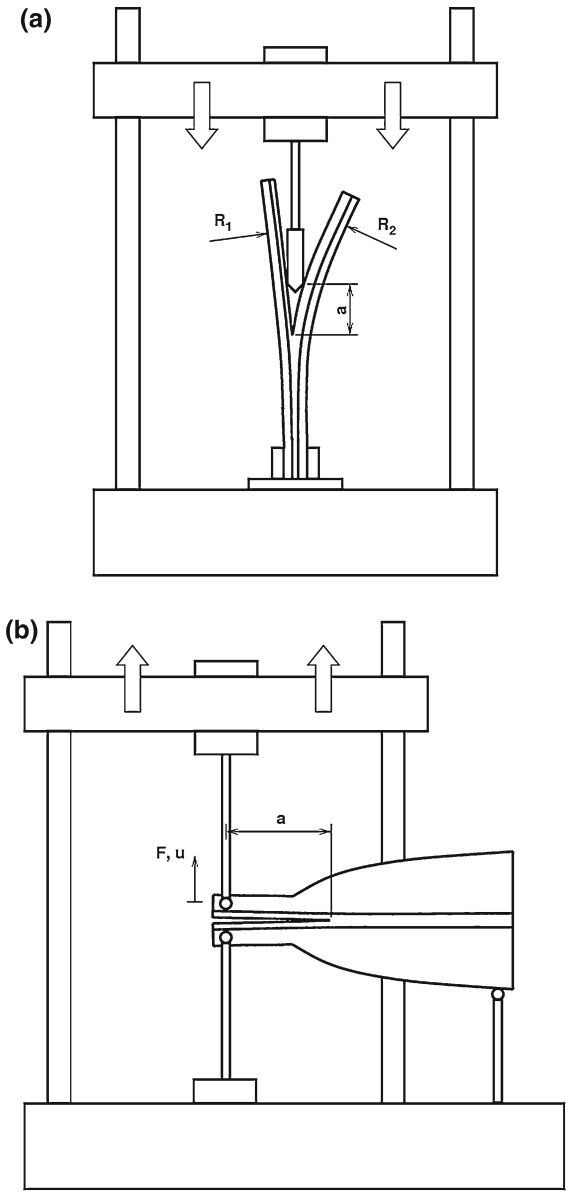

Fig. 2 The experimental set-up for **a** the EPFM wedge-peel test specimen, and **b** the LEFM tapered double-cantilever beam (TDCB) test specimen

in Table 1. The values quoted, for each specimen geometry, are the mean and standard deviation from five replicate tests, which all showed a locus of failure that was close to the centreline of the adhesive layer. This observation supports, of course, the averaging of the different radii of curvature. Table 1 reveals that the work of fracture increases with increasing thicknesses of the adhesive layer, as illustrated by the smaller radii.

Table 1 Experimental EPFM wedge-peel test results (mild-steel adherend thickness, $h = 0.78$ mm)

h_{adh} (mm)	R_a (mm)
0.08	186 ± 14
0.18	128 ± 27
0.24	110 ± 4

Locus of joint failure was cohesive through the adhesive layer and near the centreline

2.3 LEFM TDCB tests

The mode I adhesive fracture energy, G_a, of the adhesive was obtained experimentally for different thicknesses of the adhesive layer using the LEFM TDCB test specimen, see Fig. 2b. These specimens were prepared and tested according to the ISO Standard 25217:2009. The adherends were first machined from bulk aluminium-alloy (grade 2014A) with a taper characterised by a value of m (see ISO 25217: 2009) equal to 2 mm^{-1}. The adherends were then subjected to grit blasting, degreasing and a chromic-acid etch. They were then bonded together and the adhesive cured, as described above, after placing steel wires with an appropriate diameter and poly(tetrafluororethylene) film in the layer to control the adhesive layer thickness, h_{adh}, and to form a pre-crack. The TDCB joints were then tested to failure using a cross-head speed of 0.2 mm/min. Stable crack propagation mainly occurred and the load, P, the cross-head displacement, u, and the crack length, a, were recorded as a function of time. From these measurements, the adhesive fracture energy, G_a, was derived as a function of the crack length according to the LEFM corrected beam theory (CBT) (Blackman et al. 2003a):

$$G_a = \frac{4P^2}{EB^2} m \left[1 + 0.43 \left(\frac{3}{ma} \right)^{1/3} \right] \tag{2}$$

where B is the width of the specimen and E is the modulus of the beam material. As a cross-check, the value of G_a was also obtained via the LEFM experimental-compliance method (ECM):

$$G_a = \frac{P^2}{2B} \frac{dC}{da} \tag{3}$$

where $C = u/P$ is the compliance, the derivative of which, dC/da, is obtained by a regression analysis of a plot of C versus a. No significant differences in the values of G_a from these two calculation methods were observed, and no significant 'R-curve' was recorded.

Table 2 Experimental LEFM TDCB test results (adherend: aluminium alloy)

h_{adh} (mm)	G_a (J/m^2)	Locus of failure
0.24	212 ± 4	
0.38	263 ± 13	Near the centreline of
0.56	226 ± 12	the adhesive layer
0.87	277 ± 42	
0.20	153 ± 3	Near the adhesive/
0.41	186 ± 15	adherend interface

The experimental values of the adhesive fracture energy, G_a, are shown in Table 2, where the average and standard deviation values are quoted. All specimens showed a locus of failure that was cohesive through the adhesive layer. The failure was near the centreline of the adhesive layer for most specimens, except for a few joints which possessed relatively thin adhesive layers where the crack path was close to one of the adhesive/adherend interfaces. These results are shown separately in Table 2. When the crack runs near the centreline of the adhesive layer, the value of G_a increases from 212 to 277 J/m^2 as the layer thickness, h_{adh}, is increased from 0.24 to 0.87 mm; and a local peak in the value of G_a occurs at an intermediate thickness of $h_{adh} \cong 0.4$ mm. However, when the crack runs in the adhesive layer, but close to one of the adhesive/adherend interfaces, the values of G_a are significantly lower.

2.4 Bulk tensile tests

The adhesive and the mild-steel adherends used to prepare the wedge-peel test specimens have been previously tested in uniaxial tension (Ferracin 2003). Bulk adhesive specimens were machined to a dumbbell shape from a 1 mm thick plate of bulk adhesive and were tested at different strain-rates ranging from 2.5×10^{-5} to 2.5×10^{-2} s^{-1}. The corresponding stress versus strain curves, see Fig. 3a, show that the adhesive exhibits little rate-dependence, some strain-hardening capacity and a relatively small fracture strain. A mild-steel specimen was machined to a dumbbell shape from a 0.78 mm-thick plate of bulk material and tested in tension. The stress-strain curve is shown in Fig. 3b up to a strain of 2%, which is the estimated upper-bound to the strain range experienced by the adherends in the wedge-peel tests.

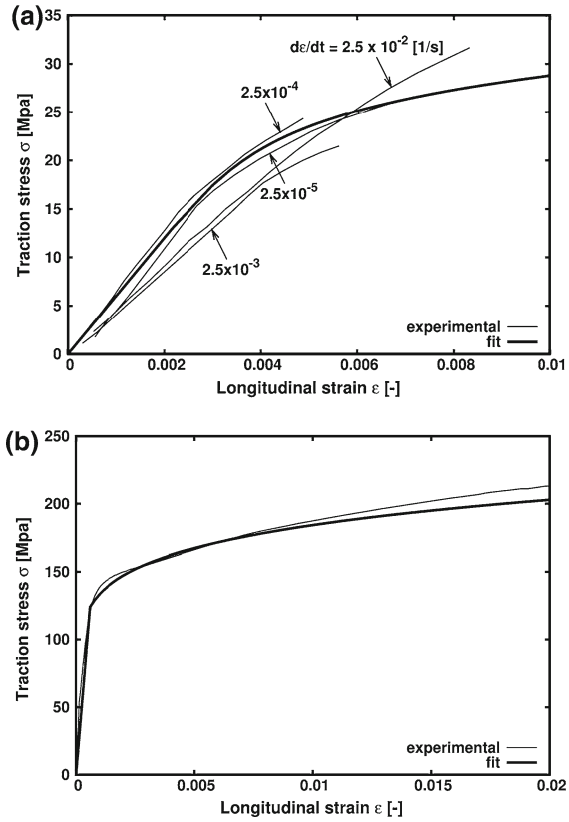

Fig. 3 The experimental tensile stress versus strain curves and corresponding fitted models for **a** the adhesive, and **b** the mild-steel adherends used for the wedge-peel tests

3 Model and numerical methods

3.1 Fundamentals of the model

A typical adhesive joint with a pre-existing crack is shown schematically in Fig. 1a. When it is loaded, damage mechanisms such as particle cleavage, particle debonding, cavitation, shear yielding, etc. take place in a region ahead of the crack tip, which irreversibly affect the integrity of the material. Depending on the adhesive system, the damage zone may remain very small, or spread over a relatively large region. The main idea behind the present model was first suggested by Needleman (1987) in the context of inclusion debonding in heterogeneous materials. It was later applied to failure in homogeneous, elastic-plastic solids by Tvergaard and Hutchinson (1992) and to rate-dependent materials by Landis et al. (2000). More recently, it has been applied to cohesive failure in

adhesive joints (Blackman et al. 2003b; Pardoen et al. 2005; Martiny et al. 2008; Salomonsson and Andersson 2008; Cooper et al. 2009). The model assumes the existence of a localised damage and deformation region immediately ahead of the crack tip called the 'fracture process zone', and the crack then propagates with such a zone immediately preceding the crack. As shown in Fig. 1b, this intrinsic 'fracture process zone' is represented by a traction versus separation condition across the crack plane, i.e. a CZM is employed. The surrounding material is considered as a continuous medium and, thus, the intrinsic damage mechanisms are extracted from the continuum medium and condensed onto a plane with zero thickness. The adhesive fracture energy, G_a, is therefore evaluated in the model, see Fig. 1b, as the sum of the energy, Γ_0, required to break the cohesive elements and of the total energy expended in the bulk of the adhesive layer, Γ_b, i.e. by inelastic deformations such as viscoplastic-energy dissipation or by locked-in elastic strain-energy.[2]. As suggested by Pardoen et al. (2005), and shown by Martiny et al. (2008), it is further assumed that the cohesive zone response is independent upon the stress-state existing in the near crack-tip region. Thus, the material parameters defined for the CZM, i.e. the peak stress, $\hat{\sigma}$, and intrinsic fracture energy, Γ_0, are considered to be material constants for a given adhesive. Therefore, any dependence of the adhesive fracture energy, G_a, upon the adhesive layer thickness, for example, can only enter through changes in the energy expended in the bulk of the adhesive layer, Γ_b. As indicated in the introduction, the assumption of using a constant value for Γ_0, which is independent of the constraint, will be discussed later in the text.

3.2 Implementation

The above modelling approach was implemented via a large-rotation, 2D plane-strain, steady-state, FEM formulation. The need for large rotations comes from the fact that, in most peel tests, including the wedge-peel test specimen, the arms of the specimen can bend appreciably, hence moving away and rotating from their original positions. The 2D, plane-strain and steady-state assumptions stem from concerns of computational efficiency, related to the very small mesh sizes needed to resolve properly the stresses in the fracture process zone.

[2] The Γ_b term was originally denoted by Γ_p by Martiny et al. (2008). This change in notation was made for clarity, and will be explained in Sect. 3.5.

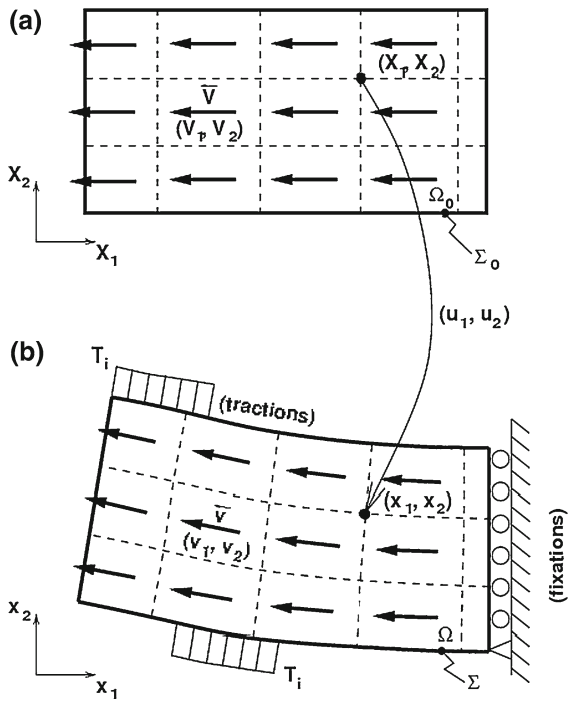

Fig. 4 The definition of the **a** undeformed, and **b** deformed configurations and associated quantities involved in the steady-state formulation

3.2.1 *The steady-state finite-element model formulation*

The present steady-state FEM formulation is an extension to the approach initially proposed by Dean and Hutchinson (1980). Consider the 2D domain depicted in Fig. 4a, which spans a volume Ω_0 enclosed by a surface Σ_0. In the steady-state regime, and in the absence of any loads, solid material is flowing through, free of any stress, from the right-hand to the left-hand side, with a uniform and constant material velocity given by:

$$\begin{cases} V_1 = -\dot{a} \\ V_2 = 0 \end{cases} \tag{4}$$

where $\dot{a}$ is a constant and corresponds to the crack velocity. This configuration is the 'reference configuration', Ω_0, in which any given point is located through a pair of coordinates (X_1, X_2). Next consider that different fixed points and loadings are applied to Σ_0, and

held constant over time. Upon completion of a transient phase, a new steady-state configuration, i.e. the 'deformed configuration', Ω, is reached, as shown in Fig. 4b. In this configuration, any given point is now located through a pair of coordinates (x_1, x_2) and the material is flowing through a different volume, Ω, with a material velocity given by:

$$v_i = \frac{\partial x_i}{\partial X_j} V_j \quad (i = 1, 2) \tag{5}$$

The deformed configuration, Ω, is unequivocally defined by the displacement field, (u_1, u_2), which maps the position of any point in the reference configuration, Ω_0, to the corresponding position in the deformed configuration, Ω:

$$x_i = X_i + u_i \quad (i = 1, 2) \tag{6}$$

The deformed configuration can be found by solving the equations of equilibrium. Therefore, the reference configuration is discretised using finite elements and the displacement field is approximated, via shape functions, from the displacement values at the nodes of the resulting mesh, which become the unknowns of the problem. The latter are then found by solving the weak form of the equilibrium conditions which, in the absence of inertial effects and volume forces, may be stated as:

$$\int_{\Omega_0} S_{ij} \delta E_{ij} d\Omega = \int_{\Sigma_0} T_i \delta u_i d\Sigma \tag{7}$$

where T_i are the tractions acting on Σ_0, and E_{ij} and S_{ij}, respectively, denote the Green-Lagrange strain-tensor and the second-order Piola–Kirchhoff stress-tensor, respectively. (This particular choice of the strain and stress makes it possible to account for large rotations, whilst integrating the equilibrium equations of the unknown deformed configuration over the undeformed configuration which is known a priori.) The Green-Lagrange strains in Eq. (7) are defined under 2D plane-strain conditions as:

$$E_{ij} = \left(\frac{\partial u_i}{\partial X_j} + \frac{\partial u_j}{\partial X_i} + \frac{\partial u_k}{\partial X_i} \frac{\partial u_k}{\partial X_j} \right) \quad (i, j = 1, 2, 3) \tag{8}$$

with $u_3 = 0$ and, hence, $E_{13} = E_{23} = E_{33} = 0$ under 2D plane-strain conditions. The second Piola–Kirchhoff stresses in Eq. (7) depend upon the strain history seen by the material particles according to a material law of the form:

$$\frac{DS_{ij}}{Dt} = f\left(E_{ij}, \frac{DE_{ij}}{Dt}, \phi_m \right) \quad (i, j = 1, 2, 3) \tag{9}$$

where ϕ_m are the state variables and D/Dt denotes the material derivation:

$$\frac{D}{Dt} = \frac{\partial}{\partial t} + V_k \frac{\partial}{\partial X_k} \tag{10}$$

Under steady-state conditions, the partial derivative with respect to time in Eq. (10) vanishes, so that Eq. (9) becomes:

$$V_k \frac{\partial S_{ij}}{\partial X_k} = f\left(E_{ij}, V_k \frac{\partial E_{ij}}{\partial X_k}, \phi_m \right) \tag{11}$$

or, by making use of Eq. (4):

$$-\dot{a} \frac{\partial S_{ij}}{\partial X_1} = f\left(E_{ij}, -\dot{a} \frac{\partial E_{ij}}{\partial X_1}, \phi_m \right) \tag{12}$$

The Piola–Kirchhoff stresses in Eq. (7) can thus be evaluated by integrating Eq. (12), in the undeformed configuration, over lines with constant X_2, i.e. streamlines, from the right boundary of the domain, corresponding to $X_1 = X_1^r$, down to the X_1 coordinate of interest:

$$S_{ij}(X_1, X_2) = S_{ij}\left(X_1^r, X_2\right) - \frac{1}{\dot{a}} \int_{X_1^r}^{X_1} f\left(E_{ij}, -\dot{a} \frac{\partial E_{ij}}{\partial X_1}, \phi_m \right) dX_1 \tag{13}$$

Equation (8) is non-linear in the displacement field and the function $f\left(E_{ij}, -\dot{a} \frac{\partial E_{ij}}{\partial X_1}, \phi_m \right)$ appearing in Eq. (13) is non-linear in the presence of plasticity, so that the equation of equilibrium, Eq. (7), needs to be solved numerically. A Newton procedure, similar to that outlined by Dean and Hutchinson (1980), is followed. Also, the integrals appearing in Eqs. (7) and (13) must be evaluated numerically. This is achieved for Eq. (7) through Gauss integration, whilst the integral in Eq. (13) is evaluated by a backward-Euler scheme. This is possible by using structured meshes only, as shown in Fig. 4a, so that the Gauss points are aligned on lines with constant X_2 values. The FEM solution is an approximation to the exact solution of the equilibrium equations. A mesh-convergence analysis is conducted for each analysis to ensure that the FEM solution, and the derived numerical results, are sufficiently close to the exact solution. This is achieved by decreasing the size of the elements successively until no significant change is observed in the numerical results.

3.2.2 The CZM formulation

The above FEM is supplemented with a CZM to simulate the behaviour of the intrinsic fracture process zone.

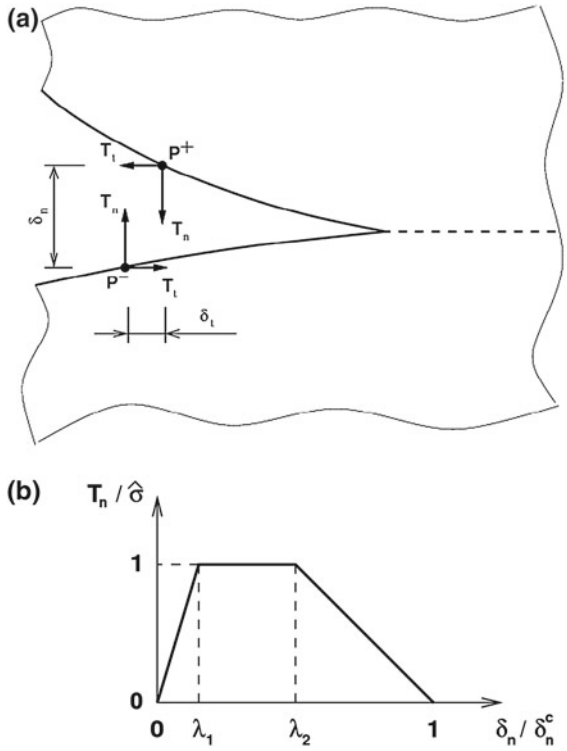

Fig. 5 **a** The definition of the quantities related to the cohesive elements, and **b** a schematic of the traction versus separation law

Considering Fig. 5a, the crack is extended ahead of the actual crack tip and prevented from opening freely in that region by the cohesive forces acting in opposite directions on each of the crack faces. The forces per unit of crack area, T_n and T_t, acting in the directions normal and tangential to the crack faces depend upon the corresponding crack-opening displacements, δ_n and δ_t, according to a particular traction versus separation relationship (e.g. see Fig. 5b).

The present model deals with cases where mode I is the predominant mode of fracture. Hence, the opening displacement in the tangential direction, δ_t, will be assumed to evolve free of any tangential force, i.e. $T_t = 0$. The only relationship that, therefore, needs to be made explicit is the dependence of the normal traction upon the normal opening displacement: $T_n = T_n(\delta_n)$. From Needleman (1987), the traction T_n is assumed to respond linearly to the opening displacement δ_n with a modulus E_n that progressively degrades as a damage parameter, d, evolves from a value of 0, in the initial, undamaged state, to a value of 1 at complete failure, when the traction drops to zero and the actual crack propagates. Thus:

$$T_n = E_n(d)\,\delta_n \tag{14}$$

The main feature of this approach is that the tractions linearly return to zero when the opening displacement decreases as shown in Fig. 5b. Following the work of Tvergaard (1990), the damage parameter, d, in Eq. (14) is evaluated as a function of time, t, so that:

$$d(t) = \max_{t' < t} \frac{\delta_n(t')}{\delta_n^c} \tag{15}$$

where δ_n^c is the critical opening displacement at which failure occurs and the variation of the modulus E_n, appearing in Eq. (14), as a function of the damage parameter, d, completely defines the behaviour of the cohesive elements.

In addition to Eq. (14), the 'virtual' crack faces ahead of the actual crack tip are prevented from interpenetrating by introducing inequalities of the form $\delta_n \geq 0$, implemented with the help of Lagrange multipliers, and added to the finite-element formulation. From a numerical point of view, the Lagrange multipliers substitute for the cohesive stresses, which are zero when $\delta_n = 0$, and locally compensate for the external loading until any interpenetration is removed.

3.3 The EPFM wedge-peel test specimen

A schematic representation of the wedge-peel test specimen is shown in Fig. 6a, along with the corresponding model in Fig. 6b. Well ahead of the crack tip, the specimen is not affected by the loading and remains undeformed. Far behind the wedge, it is completely unloaded and shows a uniform curvature. As a consequence, the model can be restricted to some distances, l_u and l_d, ahead of the crack tip and past the wedge, respectively. This necessitates the application of appropriate boundary conditions to substitute for the missing portions. The inlet section, see Fig. 6b, is clamped in order to impose zero deformation and to fix rigid-body modes at the same time. The outlet section, see Fig. 6b, should ideally be constrained so as to give a zero material derivative of the curvature. However, such conditions are difficult to formulate and to implement. It is much easier to extend the arms by a length $l_{d,ext}$ past the outlet section and let the resulting end section be free. If $l_{d,ext}$ is sufficiently large, then the outlet section is unaffected by the presence of the free end and behaves as if the arms were extending to infinity. In practice, lengths l_d and $l_{d,ext}$ are merged into a single

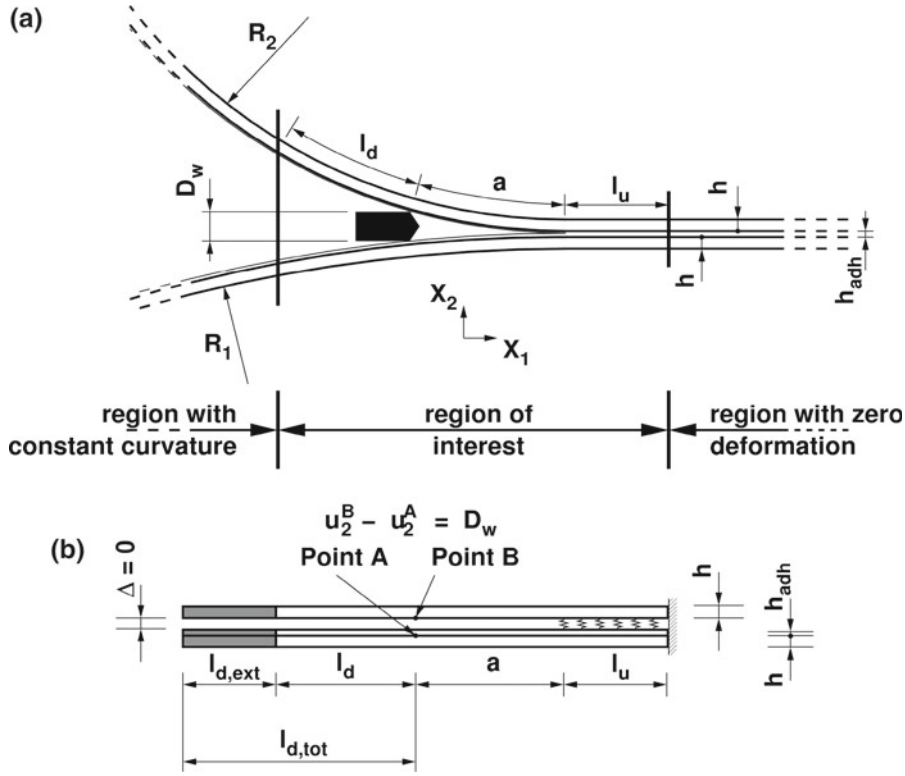

Fig. 6 **a** A schematic representation of the wedge-peel test specimen, and **b** corresponding boundary conditions used in the numerical-modelling studies

value $l_{d,tot}$ that is increased until a significant portion of the arms past the wedge show a uniform curvature. The outlet section can then equally be placed in this portion. Similarly, the length l_u is increased until the computed crack tip opening displacement remains unchanged for a given crack length and wedge thickness. The choice of these lengths is part of the convergence study which is run for all the analyses.

For the sake of simplicity, the cohesive elements are placed either along the specimen centreline when simulating test configurations failing close to the centreline of the adhesive layer, or along one of the adhesive/adherend interfaces when simulating test configurations failing close to one of these interfaces. Moreover, the extent of the cohesive elements is restricted to the region ahead of the crack tip, i.e. they span the length l_u. This significantly reduces the number of iterations in the solution procedure that would otherwise be required to break the cohesive elements. The disadvantage of this approach is that the crack length, a, is unknown a priori; and its value must be found by iteration until the condition is satisfied that the opening displacement at the assumed crack tip is indeed equal to its critical value δ_n^c. The presence of the wedge, of thickness D_w, is taken into account by imposing the following multi-point constraint:

$$u_2^B - u_2^A = D_w \tag{16}$$

where the vertical displacements u_2^A and u_2^B are taken, as an approximation, on the adhesive/adherend interfaces to avoid local strains developing in the adhesive. It should be noted that the axial component of the force imposed by the wedge, as well as the possible misalignment of points A and B in the deformed geometry, are also neglected. All of these simplifications are valid providing the thickness of the wedge, D_w, is small compared with the crack length, a. In the cases where the cohesive elements are inserted along the centreline of the specimen, only the upper half of the geometry needs to modelled due to symmetry, and the condition in Eq. (16) becomes a simple displacement boundary condition:

$$u_2^B = \frac{1}{2} D_w \tag{17}$$

Figure 7 shows a typical mesh in the case of a symmetrical model of the wedge-peel test, in the deformed configuration, corresponding to the following specimen dimensions: $h_{adh} = 0.24$ mm and $h = 0.78$ mm.

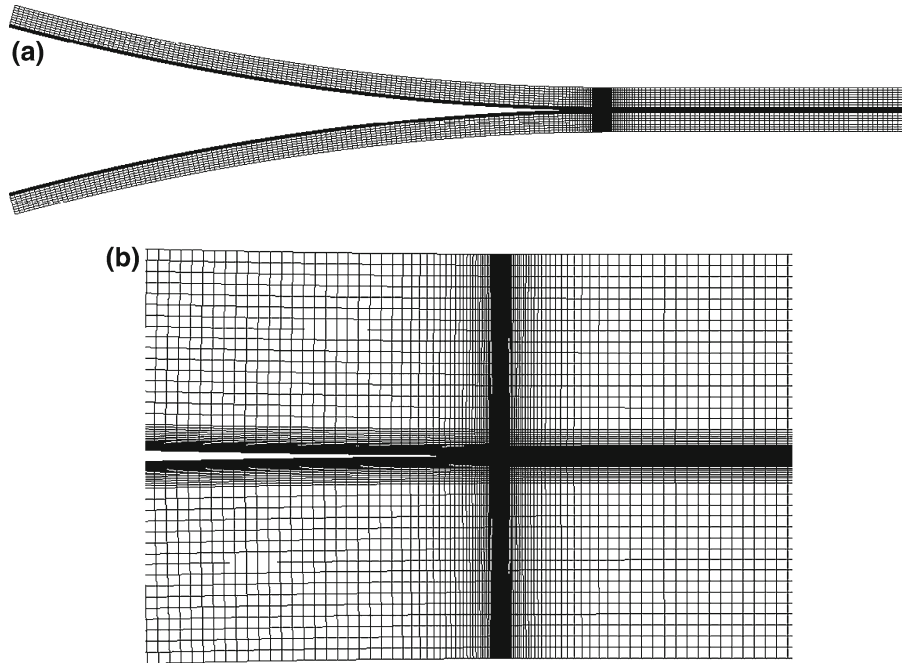

Fig. 7 **a** A typical mesh which yields accurate results for a symmetrical model of the wedge-peel test specimen, and **b** a close-up view of the crack tip region. In the case of a symmetric problem, only the upper half of the specimen is modelled

In order to capture the damage mechanisms at the crack tip, the mesh shows very fine elements in this region which are square in shape and 0.5 μm in dimension, i.e. about 1/500 times the thickness of the adhesive layer. When moving away from the crack tip, these elements are expanded, since such a fine size is no longer required. Hence, they become rectangular as their largest dimension is increasing by a geometrical progression factor of 1.1. Upon reaching the adherend, less local phenomena need to be captured. Thus, their height reaches about 50 μm, which is 1/16 times the thickness of the arms and 100 times the size of the elements at crack tip, which still produces accurate results. In total, the mesh has approximately 120,000 nodes and 40,000 elements.

3.4 The LEFM TDCB test specimen

As may be seen in Fig. 2b, the height of the beam is not constant along a TDCB test specimen. As a consequence, the geometry of the full specimen cannot be reproduced within the present steady-state formalism. However, upon focusing on the crack tip region in the adhesive material, where the fracture process and energy dissipation mechanisms take place, steady-state conditions do prevail, since both the measured rate of crack propagation and the adhesive fracture energy, G_a, reach a plateau value. Therefore, the TDCB test is modelled using an equivalent steady-state model of the wedge-peel test characterised by the same adherend material and by values for the thicknesses of the wedge and adherend such that Eq. (2), which normally applies to TDCB test specimens, still holds for a value of a equal to 200 mm, which was arbitrarily chosen to be in the range of values seen in actual TDCB tests. In practice, starting from an initial estimated value for the thickness of the arms, the wedge thickness is modified iteratively until the crack length is equal to 200 mm. The left- and right-hand sides of Eq. (2), are then evaluated and compared with each other. If they are equal to each other, the equivalent geometry has been found. Otherwise, the thickness of the arms needs to be modified, and the whole procedure repeated iteratively until Eq. (2) is fulfilled. The motivation behind the definition of the equivalent wedge-peel test specimen is that, by reproducing the same relationship between applied force and adhesive fracture energy, namely Eq. (2), as in the TDCB test specimen a similar stress-state is developed at the crack tip. This approach was validated against transient numerical simulations performed with the actual geometry of the TDCB test specimens which demonstrated that the effect of the particular choice of the arbitrarily-chosen crack length value was not significant.

3.5 Computing the adhesive fracture energy, G_a

The value of the adhesive fracture energy, G_a, is evaluated numerically from the model, see Fig. 1b, as the sum of the energy required to open the cohesive elements completely, Γ_0, and of the work expended (per unit area of crack advance) in the bulk of the adhesive layer, Γ_b,[3], i.e.:

$$G_a = \Gamma_0 + \Gamma_b \tag{18}$$

The value of Γ_0, referred to as the 'intrinsic work of fracture', is equal to the area under the traction versus separation curve. For the particular shape depicted in Fig. 5b, it is given by:

$$\Gamma_0 = \frac{1}{2}\delta_n^c \hat{\sigma}\,(1 - \lambda_1 + \lambda_2) \tag{19}$$

The value of Γ_0 is constant in the present CZM throughout all the modelling studies, since both δ_n^c and $\hat{\sigma}$ are kept constant. However, the work expended per unit area of crack advance in the bulk of the adhesive layer, Γ_b, may depend upon the stress-state prevailing in the adhesive and, hence, upon both the test specimen geometry and the test configuration. It is computed, under steady-state conditions, by integrating the material derivative of the strain energy density, W, over the adhesive layer and by dividing it by the material velocity:

$$\Gamma_b = \frac{1}{\dot{a}} \int\limits_{\Omega_{adh}} \frac{DW}{Dt} d\Omega_{adh} = \frac{1}{\dot{a}} \int\limits_{\Omega_{adh}} S_{ij} \frac{DE_{ij}}{Dt} d\Omega_{adh} \tag{20}$$

which, with Eqs. (4) and (10), becomes:

$$\Gamma_b = -\int\limits_{\Omega_{adh}} S_{ij} \frac{\partial E_{ij}}{\partial X_1} d\Omega_{adh} \tag{21}$$

When using structured meshes, as shown in Fig. 4a, the value of $\partial E_{ij}/\partial X_1$ in Eq. (21) can readily be approximated as $\Delta E_{ij}/\Delta X_1$, where ΔE_{ij} is the difference between the values of E_{ij} at successive integration points and ΔX_1 is the distance separating the latter. The value of Γ_b can be further split into two terms, i.e. the locked-in elastic strain-energy, Γ_e, and the plastic-energy dissipation, Γ_p:

$$\Gamma_b = \Gamma_e + \Gamma_p \tag{22}$$

[3] The notation departs from that used in Martiny et al. (2008). Γ_b is the total energy dissipated in the bulk of the adhesive layer, formerly denoted by Γ_p Martiny et al. (2008); and now Γ_p is limited to the plastic-energy dissipation only, in the bulk of the adhesive layer.

So that Eq. (18) now becomes:

$$G_a = \Gamma_0 + \Gamma_e + \Gamma_p \tag{23}$$

The elastic-energy locked-in the adhesive layer, Γ_e, results from non-uniform plastic deformation in the joint and is directly associated to the residual stresses, see the appendix in Wei and Hutchinson (1997). It may be readily evaluated, see Eq. (22), by subtracting the plastic-energy dissipation from Γ_b. The plastic-energy dissipation, Γ_p, is ascertained by limiting the energy increments in Eq. (21) to only the contributions from the plastic strains, E_{ij}^p:

$$\Gamma_p = -\int\limits_{\Omega_{adh}} S_{ij} \frac{\partial E_{ij}^p}{\partial X_1} d\Omega_{adh} \tag{24}$$

The term Γ_p can be broken further down, as detailed in Sect. 4.3.2, into contributions from the distinct deformation mechanisms, i.e. $\Gamma_p = \sum_i \Gamma_p^i$.

4 Results and discussion

Section 4.1 describes how the values of the different material parameters needed for the modelling studies were obtained. In Sect. 4.2, the numerical predictions are compared with the experimental data to assess the validity of the model. In Sect. 4.3, the different dissipation mechanisms contributing to the adhesive fracture energy, G_a, are identified, explained and quantified. These results are then employed in Sects. 4.4 and 4.5 to describe the variation of G_a as a function of a very wide range of test configurations for both the LEFM TDCB and EPFM wedge-peel test specimens. Finally, Sect. 4.6 compares the fracture behaviour of these two types of test specimen and their various test configurations, and comments on the relevance of our findings to (a) experimental results to be found in the literature, and (b) the basic meaning of the term the adhesive fracture energy, G_a.

4.1 Identification of the material parameters

4.1.1 Stress versus strain behaviour of the adherend materials

The constitutive behaviour of the mild-steel adherends used in the EPFM wedge-peel specimens is modelled using the rate-independent, isotropic J_2 elastoplastic

Table 3 Material properties used in the model

Material	E (GPa)	ν (–)	σ_0 (MPa)	η (–)	n (–)
Mild steel	210	0.30	124	–	0.14
Aluminium alloy	72.4	0.33	–	–	–
Epoxy adhesive	6	0.45	13	87, 000	0.13

theory where the strain increments, $d\varepsilon_{ij}$, are evaluated as the sum of the elastic (superscript e) and plastic (superscript p) strain increments, such that:

$$d\varepsilon_{ij} = d\varepsilon_{ij}^{e} + d\varepsilon_{ij}^{p} \tag{25}$$

The terms on the right-hand side are given by:

$$d\varepsilon_{ij}^{e} = \frac{1+\nu}{E} d\sigma_{ij} - \frac{\nu}{E} d\sigma_{kk} \tag{26}$$

where E is the Young's modulus and ν is the Poisson ratio of the material, and, by:

$$d\varepsilon_{ij}^{p} = \frac{3}{2} d\bar{\varepsilon}^{p} \frac{d\sigma_{ij} - \sigma_{kk}/3}{\bar{\sigma}} \tag{27}$$

where $\bar{\varepsilon}^{p}$ and $\bar{\sigma}$ denote the effective plastic strain and the effective stress, respectively, which are related to each other through the hardening law. The material parameters are therefore defined by the Young's modulus of the material, E, the Poisson ratio, ν, and a hardening law. They were determined by fitting the curve in Fig. 3b, using the least-square method, with Eq. (28):

$$\sigma = \begin{cases} E\varepsilon, & \varepsilon < \frac{\sigma_0}{E} \\ \sigma_0 \left(\frac{E\varepsilon}{\sigma_0}\right)^{n}, & \varepsilon \geq \frac{\sigma_0}{E} \end{cases} \tag{28}$$

The values of these parameters are given in Table 3 and the resulting fit is presented in Fig. 3b. The aluminium alloy used for the adherends for the LEFM TDCB specimens showed no signs of plastic deformation during the tests and was therefore modelled as a linear-elastic material, see Table 3 (Hadavinia et al. 2006).

4.1.2 Stress versus strain behaviour of the adhesive

The stress versus strain behaviour of the adhesive is shown in Fig. 3a and, since there is no significant rate dependence, the Young's modulus and hardening behaviour were determined by least-square fitting all of these curves to the following equation:

$$\sigma = \begin{cases} E\varepsilon, & \varepsilon < \frac{\sigma_0}{E} \\ \sigma_0 \left[1 + \eta \left(\varepsilon - \frac{\sigma}{E}\right)\right]^{n}, & \varepsilon \geq \frac{\sigma_0}{E} \end{cases} \tag{29}$$

It should be noted that Eq. (29) makes use of the Swift hardening-law and, compared with Eq. (28), it has an additional material parameter, η, which enables a better match to the experimental curves. Figure 3a reveals a good agreement between Eq. (29) and the experimental measurements, and the values of the material parameters used are given in Table 3.

4.1.3 Identification of the CZM parameters

The traction versus separation law characterising the fracture process in the adhesive is difficult to measure directly, since the fracture phenomena take place at a very small-scale that is difficult to isolate experimentally while imposing a stress state similar to the one occurring at a crack tip. Also, the traction versus separation law represents the overall effect of the fracture process, and is not intended to reproduce its exact details. Hence, an assumption is made about its shape, to limit the number of parameters to be identified, and the defining material parameters are determined indirectly by inverse analysis. This approach has been previously successfully adopted by Pardoen et al. (2005) and Salomonsson and Andersson (2008).

The particular shape used by Tvergaard and Hutchinson (1992) has been chosen for the present work for its simple, piece-wise linear definition. It corresponds to Fig. 5b with $\lambda_1 = 0.15$ and $\lambda_2 = 0.50$. The only two remaining parameters to be identified are δ_n^c, the critical opening displacement at which the tractions drop to zero, and, $\hat{\sigma}$, the peak stress, i.e. the 'strength' of the fracture process zone. These are assumed to be stress-state independent and, hence, will be kept constant when the two different test specimens, and all their many different test configurations, are modelled, see below. Therefore, they have been determined by minimising the overall mismatch between the numerical predictions and experimental values over the full range of test specimens and test configurations for which experimental data are readily available, and which consist of three EPFM wedge-peel and six LEFM TDCB test results, see Tables 1 and 2. When the locus of joint failure was near the centreline, the cohesive elements

were placed along the centreline of the adhesive layer, and when near the adhesive/adherend interface they were located at the interface, see Tables 1 and 2. The mismatch has been evaluated as the maximum relative error between the experimental value, X_i^{exp}, of the average radius of curvature (in the case of the wedge-peel test specimens), or of the adhesive fracture energy (in the case of the TDCB test specimens), and the corresponding numerical prediction, X_i^{num} amongst these nine test specimens/test configurations, such that:

$$\phi = \max_i \left| \frac{X_i^{num}}{X_i^{exp}} - 1 \right| \quad (i = 1, 2, \ldots, 9) \tag{30}$$

The pair of values $\left(\delta_n^c, \hat{\sigma}\right)$ that minimizes ϕ was found with the assistance of the general-purpose in-house optimization software Minamo (2010), which is based on genetic algorithms. The above procedure gave a value of δ_n^c equal to 1.9 μm and a value of $\hat{\sigma}$ equal to 87 MPa, and from Eq. (19), these yield a value for the intrinsic work of fracture, Γ_0, equal to 112 J/m^2. It is noteworthy that the sensitivity analysis showed that a variation of ±1% in δ_n^c and in $\hat{\sigma}$ resulted in a change in the numerically-predicted values of the average radius of curvature, or the adhesive fracture energy, by ±1%; and when this variation was changed to ±5% the change in the latter two quantities was ±10%. Thus, in the present work, the values of $\hat{\sigma} = 87$ MPa and $\Gamma_0 = 112$ J/m^2 will now be kept constant for all the subsequent numerical-modelling studies.

4.2 Comparison with the experimental results

4.2.1 The EPFM wedge-peel tests

Figure 8a compares the numerically-predicted values of the average radius of curvature as a function of the thickness of the adhesive layer, h_{adh}, with the corresponding experimental values for the EPFM wedge-peel tests, which all possessed an adherend arm thickness, h, of 0.78 mm. In all these specimens failure occurred close to the centreline of the adhesive layer and, therefore, the symmetric model was used in which the crack was forced to run along the centreline of the adhesive layer. The current model accurately predicts the change of the radius of curvature as a function of the adhesive layer thickness, and the numerical predictions are all within $\frac{\Delta R_a}{R_a} = 10\%$ of the experimental values.

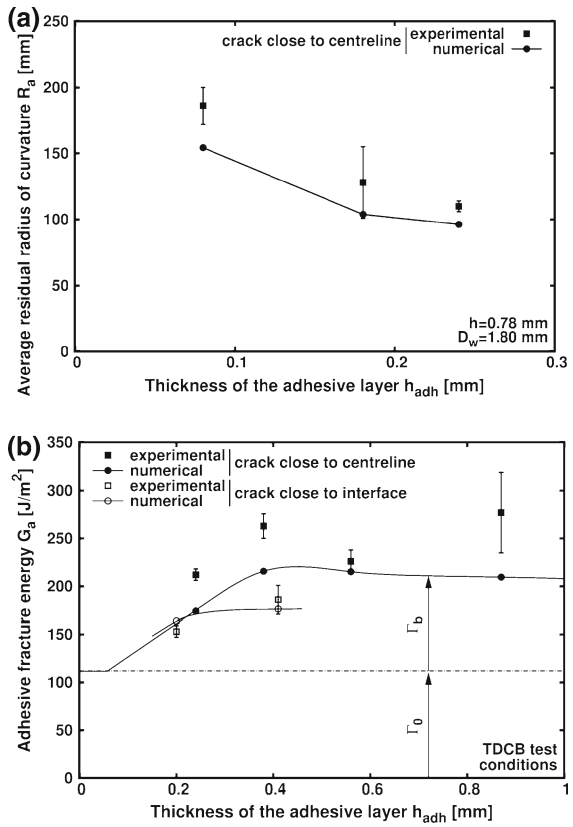

Fig. 8 Comparison between the experimental and numerically-predicted values obtained **a** from the EPFM wedge-peel test specimen, and **b** from the LEFM TDCB test specimen

4.2.2 The LEFM TDCB tests

Figure 8b shows the comparison between the experimental and predicted values of the adhesive fracture energy, G_a, as a function of the thickness of the adhesive layer, h_{adh}, for the LEFM TDCB test specimens quoted in Table 2. The energy dissipation in the bulk of the adhesive layer, Γ_b, varies with a change in the value of h_{adh} and is about 35–50% of the experimentally-measured values of G_a; whilst the intrinsic work of fracture, Γ_0, which is, of course, constant in value is responsible for the remaining contribution to the value of G_a.

In Fig. 8b there are several other noteworthy features. Firstly, for the TDCB specimens where the crack propagated near the centreline of the adhesive layer, the experiments were again modelled by forcing the crack to run along the centreline of the specimens. The corresponding numerically predicted values of

G_a accurately reflect the variation of G_a with h_{adh} that was observed experimentally, namely a steady increase up to a plateau value after passing through a small local peak at an intermediate thickness of $h_{adh} \cong 0.40$ mm. However, the numerically-predicted values all lay below the corresponding experimental values by a maximum of about 15%, which reveals that the model tends to underestimate the energy dissipation. Secondly, the TDCB specimens, where the crack propagated close to one of the adhesive/adherend interfaces, were modelled by forcing the crack to run exactly along one of the adhesive/adherend interfaces. The corresponding numerically-predicted values of G_a are again in excellent agreement with the experimental values. Thus, the model is also capable of predicting the observed decrease in G_a when the crack runs close to one of the adhesive/adherend interfaces. This success of the model in this respect arises from a decrease in the energy dissipation in the bulk of the adhesive layer, Γ_b, and this is associated with the zones of plastic-energy dissipation in the adhesive layer not being allowed to fully develop on both sides of the crack plane when the crack is very close to the adherend.

4.3 Analysis of the different contributions to the adhesive fracture energy G_a

The results discussed above have shown a very good agreement between the experimental measurements and the numerical predictions for the two very different types of test specimen, and for a wide range of thicknesses of the adhesive layer. These observations validate the proposed modelling approach which will now be used (a) to explore other test configurations, and hence (b) to address the effects of constraint of the adhesive layer, imposed by the presence of the relatively high modulus adherends. In order to limit the scope of the present paper, only test configurations where the crack propagates through the adhesive layer near the centreline will be discussed.

4.3.1 Locked-in elastic strain energy Γ_e

Figure 9 shows the calculated elastic energy that is locked-in the adhesive layer, Γ_e, versus the plastic-energy dissipation, Γ_p, for both the LEFM TDCB and EPFM wedge-peel tests, and the results cover a far wider range of test configurations than was tested experimentally. For instance, in the modelling studies the values of the adherend thickness, h, in the wedge-peel test was varied from 0.78 to 32 mm and the thickness of the wedge was varied from 0.9 to 3.6 mm. The results show that Γ_e scales linearly with Γ_p. Nevertheless, the contribution from the relatively low values of Γ_e is only 16% of Γ_p (i.e. no more than about 8% of the adhesive fracture energy, G_a) regardless of the specimen geometry and test configuration. The plastic-energy dissipation term, Γ_p, thus dominates the contribution to G_a of the work expended per unit area of crack advance in the bulk of the adhesive layer, Γ_b, as may be seen from Eq. (22).

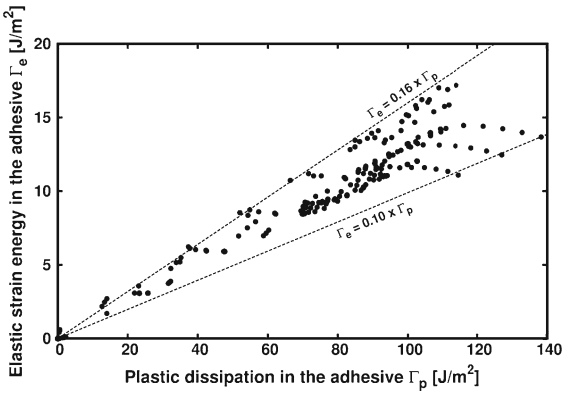

Fig. 9 The predicted locked-in elastic energy the adhesive as a function of the plastic dissipation in the adhesive layer, for the two specimen geometries and the different test configurations

4.3.2 Contributions to the plastic-energy dissipation Γ_p

Introduction Figure 10a shows a typical spatial distribution of the plastic-energy dissipation within the upper half of the adhesive layer for a LEFM TDCB test specimen with an adhesive layer thickness of 0.24 mm. The contours of the regions of active plasticity where the plastic strain-rate is non-zero are shown, together with the magnitude of the associated plastic dissipation. The regions where only elastic behaviour occurs are represented in white.

Three distinct zones of plastic-energy dissipation may be identified. Two of these, i.e. 'Zone A' and 'Zone B', have already been identified and discussed by Martiny et al. (2008) for a different (i.e. relatively high toughness) adhesive. Zone A shows intense plastic-energy dissipation, slightly above and ahead of the

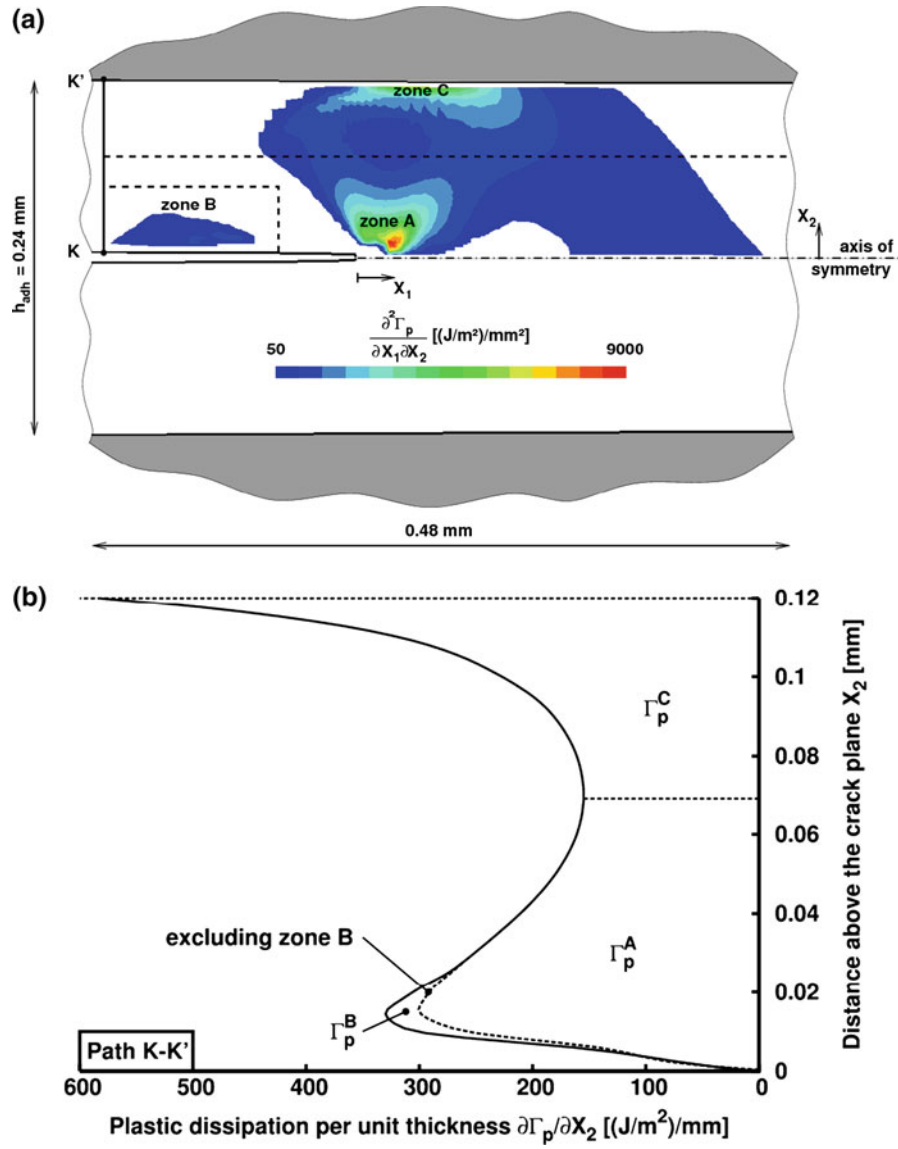

Fig. 10 Modelling results for the adhesive layer in the LEFM TDCB test specimen: **a** spatial distribution of the plastic-energy dissipation, and **b** the resulting distribution in the thickness direction (results are shown for the upper symmetrical part of the specimen only)

crack tip and fans out towards the adhesive/adherend interface. Zone B shows much less intense plastic-energy dissipation and extends, behind the crack tip, close to the crack face. The new zone observed in the present analysis, 'Zone C', shows a maximum in the plastic-energy dissipation at the adhesive/adherend interface, approximately directly above the crack tip, and spreads out in the direction of the crack plane both towards regions located ahead and behind the crack tip. Zone C merges with Zone A at approximately the mid-distance from the crack plane. Figure 10b shows the aggregated distribution of plastic-energy dissipation in the thickness direction obtained by integrating the spatial distribution of Fig. 10a along horizontal lines from far ahead of the crack tip down to the section K–K′. Plastic work is dissipated over the full thickness of the adhesive layer, although the thin layer of material located right above the crack plane does not seem to contribute significantly. Zone A and Zone C each involve a maximum in the plastic dissipation slightly above the crack plane and just below the adhesive/adherend interface, respectively. The adhesive material located in between these regions also shows significant plastic-energy dissipation, with one zone gaining in intensity as the other dies away.

The total plastic-energy dissipation, Γ_p, can be broken down by considering separately the three contributions from Zones A, B and C. Hence, Eq. (23) becomes:

$$G_a = \Gamma_0 + \Gamma_e + \Gamma_p^A + \Gamma_p^B + \Gamma_p^C \tag{31}$$

The energy contribution from Zone B, Γ_p^B, is obtained by limiting the domain of integration in Eq. (24) so as to encompass Zone B completely, and by excluding Zones A and C. Such a domain is illustrated by the dotted line around Zone B in Fig. 10a. Upon removal of the contribution of Zone B, the spatial distribution of Γ_p of Fig. 10b is modified as shown by the dotted line labelled as 'excluding Zone B'. The energy contribution of Zone A, Γ_p^A, is then estimated by integrating the modified curve from the crack plane up to its local minimum as shown by the horizontal dotted lines in Fig. 10a, b. The energy contribution from Zone C, Γ_p^C, is then ascertained in a similar manner by integrating the modified curve from its local minimum up to the adhesive/adherend interface. (This approximation had to be introduced, since Zones A and C merge together and it is therefore not possible to isolate rigorously their individual contributions, which is needed in order to quantify the separate physical mechanisms of plastic-energy dissipation in the adhesive layer).

Origin of Zone A The stress components along the semi-circular path L–L′ about the crack tip are plotted in Fig. 11a and compared with the asymptotic crack-tip field obtained semi-analytically by Drugan et al. (1982) in the particular case of an elastic-ideally plastic solid under steady-state, mode I crack propagation.[4] For angles below 170°, the agreement between the two predictions is excellent, which proves that the plastic dissipation in Zone A can be attributed to the crack-tip stress-field. Zone A will be therefore referred to as 'crack tip plasticity'. Moreover, as can be seen in Fig. 10a, Zone A spans an angular sector ranging from about 0 to 125–130° immediately followed by an elastic sector, which is also in agreement with the results of Drugan et al. (1982). This phenomenon is typical of propagating cracks, since stationary cracks show plasticity at all angles, as has been established by Rice (1967).

[4] For consistency purpose, the stresses obtained in the present study are divided by a reference value of 30 MPa which is the estimated yield stress of the adhesive material had the stress-strain curves in Fig. 3a been fitted with an elastic-ideally plastic equation.

Origin of Zone B The existence of Zone B also agrees with the results of Drugan et al. (1982). They calculated that the elastic sector following Zone A was itself followed by a second plastic sector, ranging from 160 up to 180°. They attributed this extra plastic sector to reverse plastic loading, i.e. 'reverse plasticity'. Figure 11b shows, along the streamline M–M^{IV} passing through Zone B, the variation of the deviatoric stress in the direction parallel to the crack plane, $s_{11} = (2\sigma_{11} - \sigma_{22} - \sigma_{33})/3$, as a function of the corresponding deviatoric strain component, $e_{11} = (2\varepsilon_{11} - \varepsilon_{22} - \varepsilon_{33})/3$. These are obtained by removing any hydrostatic pressure contribution from the total stress and strain tensors. The tensorial equations of plasticity, see Eqs. (25)–(27), become scalar, i.e. the σ_{kk} term vanishes, when they are expressed in terms of the deviatoric components:

$$de_{ij} = \frac{1+\nu}{E} ds_{ij} + \frac{3}{2} ds_{ij} \frac{d\bar{\varepsilon}^p}{\bar{\sigma}} \tag{32}$$

which simplifies the interpretation of the stress versus strain variations. Ahead of the crack tip, the material is stretched in the X_2 direction due to the opening of the joint with a lateral contraction in the X_1 direction, due to the Poisson effect. The value of e_{11} is thus negative up to point M′, see Fig. 11b. At the same time, s_{11} varies, first linearly with e_{11} (up to point M) and then non-linearly (up to point M′) as regions of the material enter the highly stressed region around the crack tip where the material deforms plastically. Completely past the crack tip, up to point M″ in Fig. 11b, the material essentially unloads, and s_{11} returns to zero while e_{11} retains a non-zero negative value due to the compressive plastic strains that developed between point M and point M′. Past point M″, the magnitude of this permanent deformation is decreased as part of a stress and strain redistribution process over the full thickness of the adhesive layer and adjacent adherend. This process first proceeds elastically, up to point M‴, but then develops tensile plastic-strains which gives rise to Zone B to compensate for the compressive plastic-strains that were accumulated between point M and point M′. From this process comes the phenomenon of 'reverse plastic loading'.

Origin of Zone C Plastic-energy dissipation in Zone C arises from the relatively large shear stresses which develop at the adhesive/adherend interface, approximately directly above the crack tip. Figure 12 provides a schematic representation of the mechanism responsible for such plastic deformation. Namely, as a result

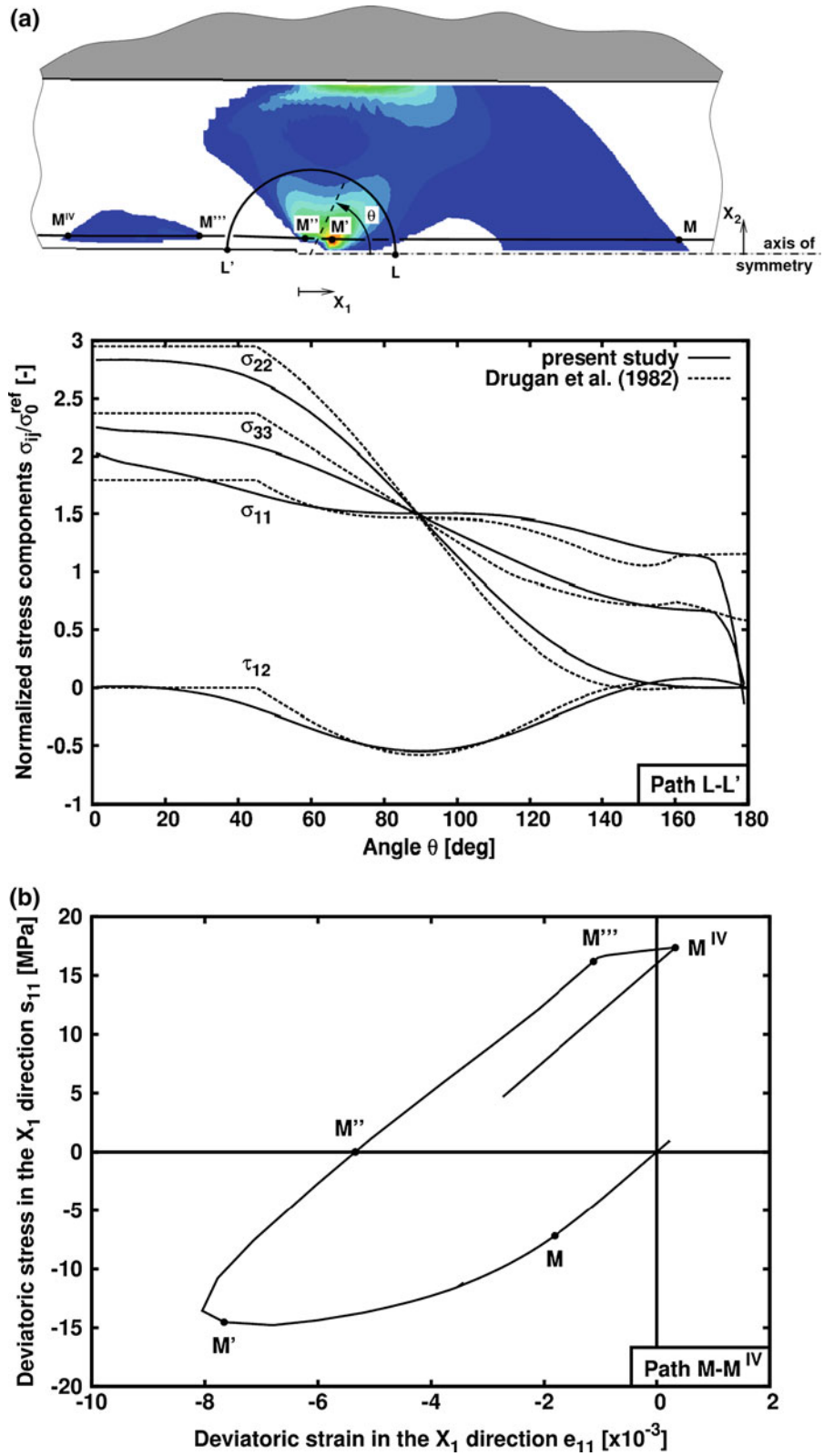

Fig. 11 The predicted typical stress distributions responsible for the appearance of **a** Zone A, and **b** Zone B [in (**a**) a comparison with the analysis by Drugan et al. (1982) is shown]

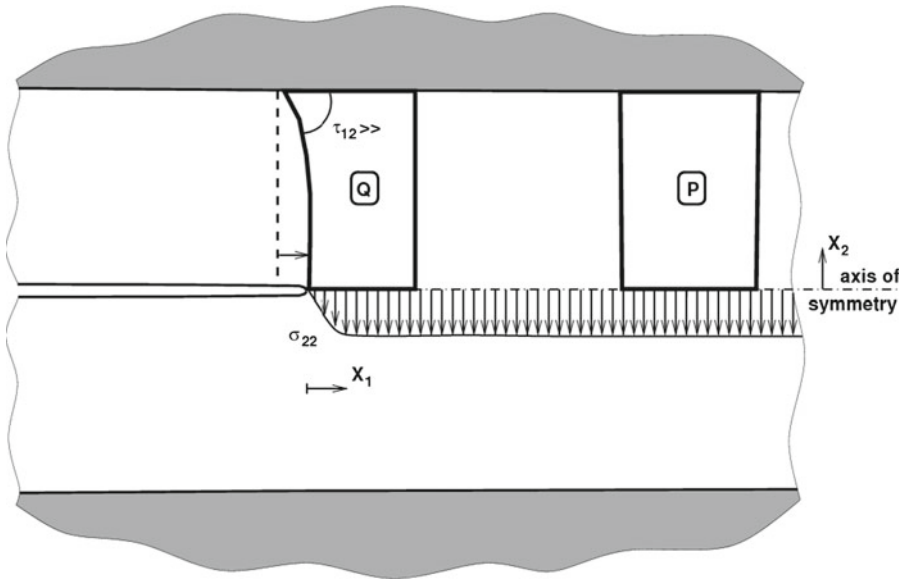

Fig. 12 A schematic representation of the deformation mechanism responsible for the appearance of Zone C

of the opening of the adhesive joint, the material ahead of the crack tip is loaded in tension in the X_2 direction. Due to the Poisson effect, the adhesive tends to contract in the lateral, X_1 direction. Considering the material volume P in Fig. 12, it is constrained by the material on both the left and right boundaries involving a near uniaxial deformation state. Hence, there is no possible net lateral contraction. If we now consider the material volume element Q of Fig. 12, its left boundary is interacting with a region where unloading takes place in the direction of the opening of the joint, and is thus allowed to contract laterally. Although, this contraction is still hindered in the vicinity of the perfectly-bonded interface since the adherend is much stiffer than the adhesive. Thus, this difference in contraction in volume Q, between its upper region down to its lower region, induces relatively large shear strains and stresses in the top-left corner of the volume Q; and these are responsible for the appearance of Zone C, as illustrated in Fig. 12.

4.4 Parametric modelling of the adhesive fracture energy, G_a, for the LEFM TDCB test

4.4.1 Effect of the thickness of the adhesive layer, h_{adh}

Introduction Figure 13a shows the numerically-predicted values of the adhesive fracture energy, G_a, as a function of the thickness of the adhesive layer, h_{adh}, for

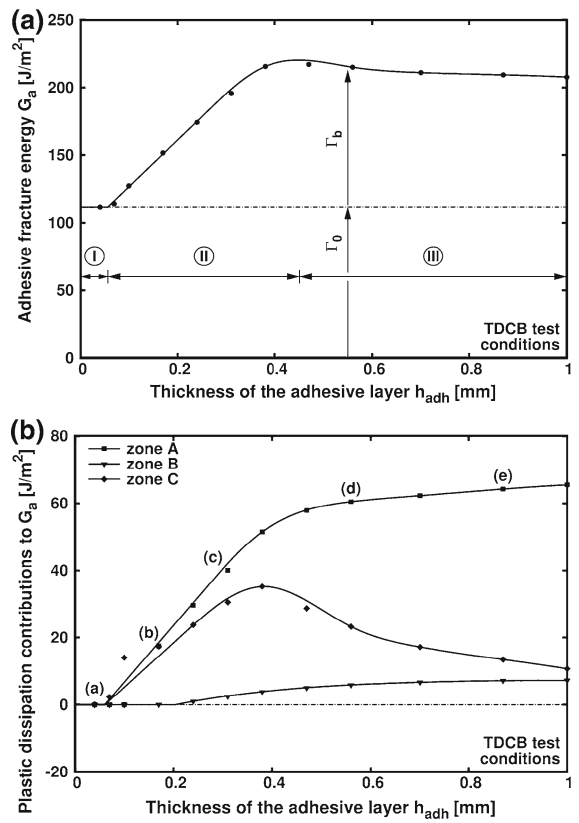

Fig. 13 The predicted **a** adhesive fracture energy, G_a, as a function of the thickness of the adhesive layer, h_{adh}, for the LEFM TDCB test specimen, and **b** contributions from Zones A, B and C to the plastic-energy dissipation to the value of G_a, again as a function of h_{adh}

the LEFM TDCB test, with the crack running along the centreline of the adhesive layer. Three distinct regimes (denoted by I, II and III) are identified. In Regime I, for very thin layers below $h_{adh} \cong 0.05\,\text{mm}$, the value of G_a is constant and is at its lowest value. In Regime II for thicker layers, up to $h_{adh} \cong 0.45\,\text{mm}$, the value of G_a increases first linearly and then reaches a peak. In Regime III, for $h_{adh} > 0.45\,\text{mm}$, the adhesive fracture energy decreases somewhat at first and then reaches a plateau value with a magnitude significantly larger than the lowest value which is exhibited for very thin adhesive layers. In previous experimental studies, Regime I has been observed by Chai (1986, 1988), and Regimes II and III by Bascom et al. (1975), Kinloch and Shaw (1981) and Chai (1986).

Figure 13b shows the actual plastic-energy dissipation in each of the three zones (i.e. Zones A, B and C, see Fig. 10) which, when all added to the value of Γ_0, give most of the adhesive fracture energy, G_a. The plastic-energy dissipation associated with Zone B is negligible. Therefore, the present discussions will focus on the contributions arising from Zones A and C to explain the results shown in Fig. 13a. In Regime I, these contributions are zero, so G_a is constant and equal to Γ_0, see Eq. (18). In Regime II, both Γ_p^A and Γ_p^C increase with increasing thickness of the adhesive layer, hence the value of G_a increases. Finally, in Regime III, Γ_p^A becomes constant, whilst Γ_p^C reverts to zero, which explains why G_a decreases very steadily with increasing h_{adh} and reaches a plateau value which is significantly higher than Γ_0.

Considering the separate role of the three zones of plasticity, Fig. 14 shows the spatial distribution of the plastic dissipation in the adhesive for the data points labelled from (a) to (e) in Fig. 13b. In Regime I, see point (a), there is no plastic-energy dissipation. In Regime II, see points (b) and (c), Zones A and C are merged and, together, span the full thickness of the adhesive layer. As the adhesive layer thickness is increased, they have more material available in which to develop, with their dimensions scaling with h_{adh}. This is associated with an increase in the plastic-energy dissipation terms, Γ_p^A and Γ_p^C. These observations agree with the explanation of Kinloch and Shaw (1981) for Regime II. Namely, that the adhesive layer is fully plastic across its height and the value of G_a increases with increasing thickness, since there is now more adhesive material in which plastic-energy dissipation may occur. Looking in more detail at points (b) and (c) in Fig. 14, the intensity of the plastic dissipation in Zone A increases as the layer becomes thicker, whilst that in Zone C decreases. This effect explains why Γ_p^A and Γ_p^C are not directly proportional to h_{adh}, and why the increase in Γ_p^A is slightly larger than for Γ_p^C. In Regime III, see points (d) and (e), Zones A and C start separating. As a consequence, their dimensions do not scale with h_{adh} anymore. In particular, the extent of Zone A stabilises so that the value of Γ_p^A levels out while Zone C and, hence, Γ_p^C tends to vanish. Once more, these observations agree with the explanation suggested by Kinloch and Shaw (1981) for Regime III, who concluded that the adhesive layer is not fully plastic in Regime III.

From the above, several noteworthy points arise. Firstly, in the present work, and in the previous work of Kinloch and Shaw (1981), all the criteria for the TDCB test to meet the requirements of following the principles of LEFM are readily met: clearly the use of the relatively thick, high yield-stress aluminium-alloy adherends in the TDCB adhesive joint basically ensures that such requirements are satisfied. Secondly, considering some suitable 'intrinsic' length scale to compare with the range of h_{adh} values that were employed, which typically were between 0.2 and 0.9 mm, then the size of the plastic zone in a bulk specimen of the adhesive has been suggested as the most obvious such parameter. Indeed, the previous work has shown that the peak in the value of G_a occurs when the thickness of the adhesive layer becomes approximately equal to twice the radius of the plastic zone in a bulk specimen under plane-stress conditions. That is, when:

$$h_{adh} = \frac{1}{\pi}\frac{EG_{Ic}}{\sigma_t} \tag{33}$$

where E is the Young's modulus, G_{Ic} is the adhesive fracture energy for a bulk sample and, σ_t is the yield stress in tension. Now the value of G_{Ic} may be estimated from Fig. 13a to be about 205 J/m^2, i.e. the value of G_a that would be expected for very thick adhesive layers. Therefore, taking σ_t to be equal to 30 MPa, then Eq. (33) gives a thickness for the adhesive layer at the peak value of G_a to be about 0.45 mm. Indeed, this is in very good agreement with the value of h_{adh} for the position of the peak, see Fig. 13a. Finally, the present work provides a better insight into the explanation offered by Kinloch and Shaw (1981) for the decrease in the value of G_a that follows this peak. They suggested that it resulted from a lower degree of constraint

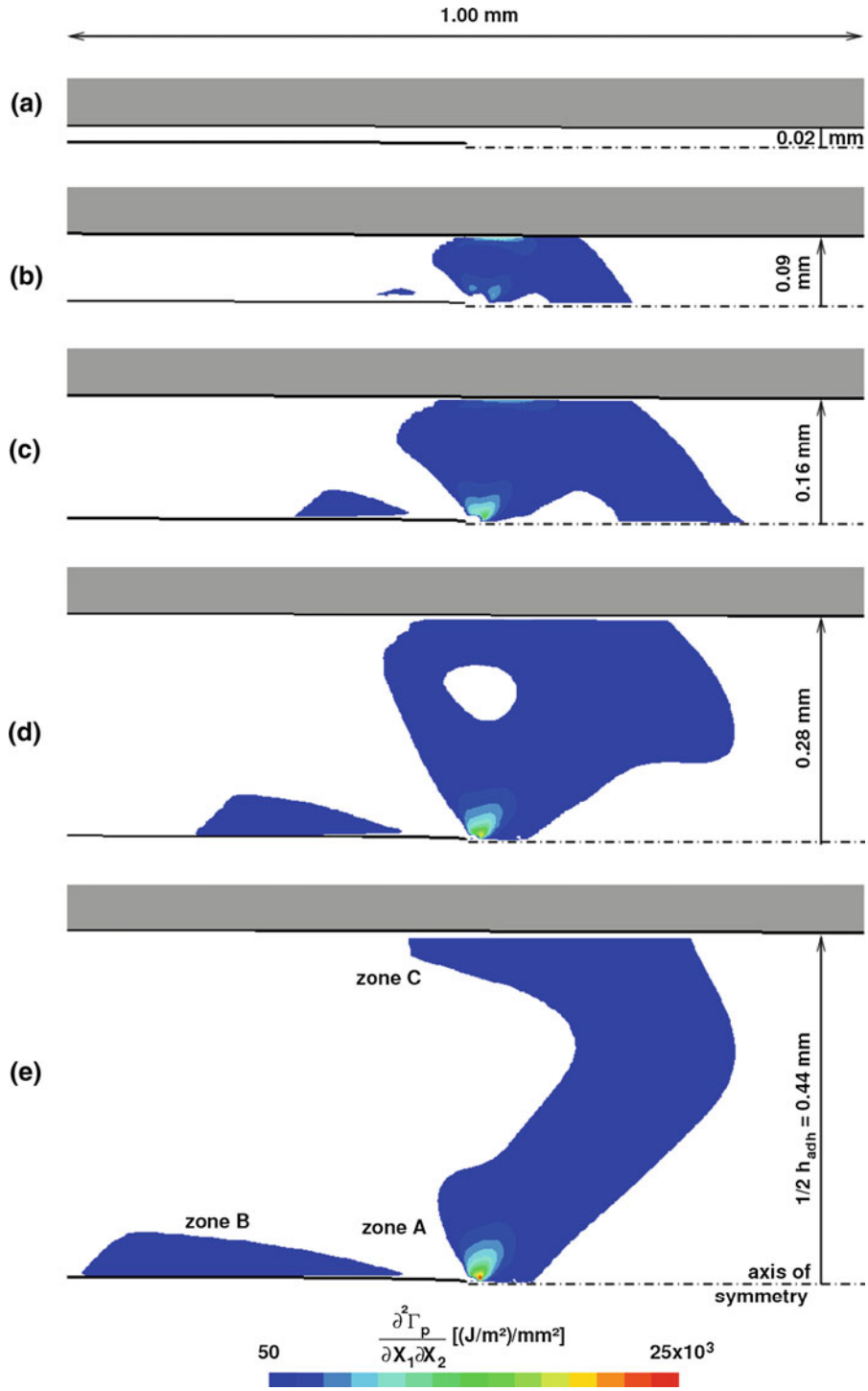

Fig. 14 The predicted spatial distribution of the plastic-energy dissipation within for the LEFM TDCB test specimens, with an adhesive layer thickness, h_{adh}, of: **a** 0.04 mm, **b** 0.17 mm, **c** 0.31 mm, **d** 0.56 mm, and, **e** 0.87 mm (results are shown for the *upper part* of the specimens only)

imposed by the adherends and, hence, a smaller plastic zone in the plane ahead of the crack tip. However, whilst there is an important role of the degree of constraint, the present study suggests that the explanation is more complex than envisaged by Kinloch and Shaw (1981).

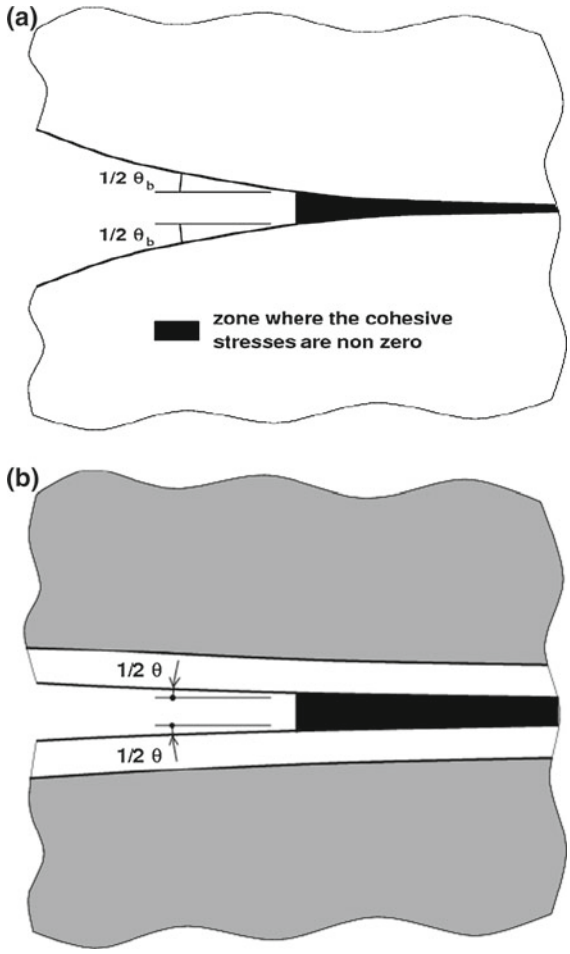

Fig. 15 A schematic description of the opening angle of the cohesive zone at crack tip **a** in bulk conditions, and **b** when the presence of the high-modulus adherends limits the deformation in the adhesive

Constraint effects When constrained between the two high-modulus adherends, the adhesive is not allowed to deform freely, as it would in a bulk sample. Indeed, it deforms less due to the far higher stiffness of the adherends, which introduces an additional constraint effect. Obviously, the thicker the adhesive layer, then lower is the degree of constraint on the crack plane and, in particular, at the crack tip. Taking the opening angle of the cohesive zone at the crack tip, θ, as a measure of the deformation at the crack tip, see Fig. 15, the corresponding constraint factor, f, may be defined as:

$$f = 1 - \frac{\theta}{\theta_b} \tag{34}$$

where θ_b is the predicted value of θ in a bulk specimen under small-scale yielding conditions. It follows from

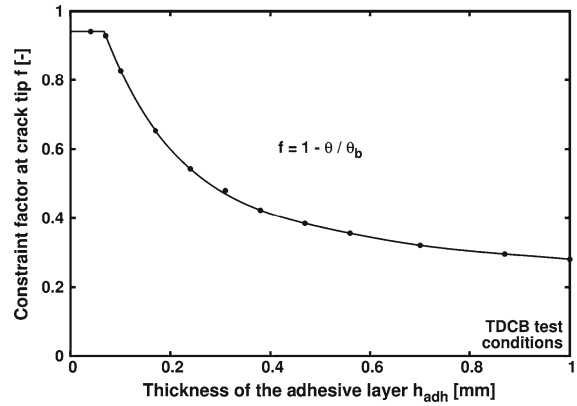

Fig. 16 The predicted constraint factor at the crack tip, f, as a function of the thickness of the adhesive layer, h_{adh}, for the LEFM TDCB test specimen

Eq. (34) that f is equal to 0 in a bulk specimen where the adhesive deforms freely, and that it progressively tends to 1 as the adhesive layer is forced to follow the more rigid deformations of the adherends, see Fig. 15a, b. In Fig. 16 the values of the constraint factor, f, have been calculated from Eq. (34), corresponding to the tests that were modelled in Fig. 13. It is of interest to note that, as for the data shown in Fig. 13, again three regimes may be distinguished.

Firstly, considering the effects of constraint on the development of Zone A, then for very thin adhesive layers, the constraint factor is very high and nearly constant. According to the definition of f, this means that the adhesive is subject to a very high degree of triaxial stresses. Thus, plastic deformation in the adhesive is severely inhibited to such an extent that the term Γ_p is equal to zero. With increasing thickness of the adhesive layer, the value of f decreases rapidly and, therefore, plastic deformation can more readily develop and Γ_p^A increases rapidly. For a thickness of the adhesive layer of 0.6 mm, and above, the constraint factor attains a minimum, plateau value. Hence, the extent of plastic deformation in Zone A is now uninhibited by the presence of the adherends, and the value of Γ_p^A also attains a plateau value.

Secondly, considering the effects of constraint on the development of Zone C, the gradient of the constraint from the crack tip to the adhesive/adherend interface must be taken into account. This aspect was discussed in Sect. 4.3.2, where it was shown that this gradient is responsible for the appearance of Zone C, since the adhesive is allowed to contract in the direction

parallel to the crack plane to a greater extent near the crack tip than at the adhesive/adherend interface. For very thin layers, i.e. $h_{adh} \leq 0.05$ mm, this gradient of constraint is small, since the constraint is very high both at the crack tip and at the adherend/adhesive interface. As a consequence, Zone C does not develop, see Fig. 14a, and the associated plastic-energy dissipation, Γ_p^C, is zero, see Fig. 13b. For thicker layers, $h_{adh} > 0.05$ mm, the constraint decreases somewhat at the crack tip and remains high at the adhesive/adherend interface due to the nearby presence of the high-modulus adherend. This creates a significant gradient of constraint which causes the appearance of Zone C, see Fig. 14b–e, and the corresponding energy contribution, Γ_p^C, to the adhesive fracture energy, see Fig. 13b. However, for thicknesses of the adhesive layer above 0.25 mm, this gradient of constraint decreases since the distance from the crack tip to the adhesive/adherend interface increases whilst the constraint at the crack tip attains a plateau. As a consequence, Zone C progressively vanishes, see Fig. 14b–e, and Γ_p^C returns to zero for relatively thick adhesive layers, see Fig. 13b.

The above explanations refine the analysis of Kinloch and Shaw (1981) and illustrate the importance of considering the distribution of the degree of constraint within the adhesive layer, as opposed to focusing on a single value taken at a particular location.

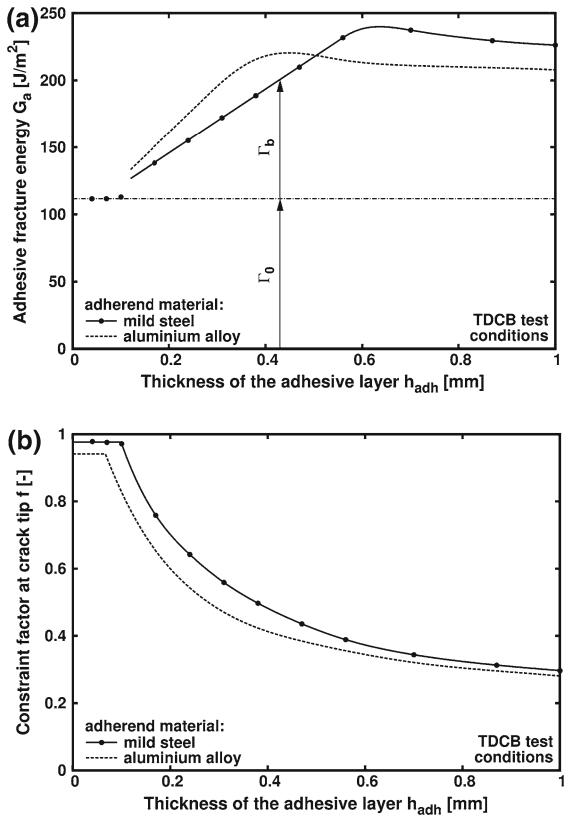

Fig. 17 The predicted **a** adhesive fracture energy, G_a, as a function of the thickness of the adhesive layer, h_{adh}, and **b** constraint factor at the crack tip as a function of the thickness of the adhesive layer, h_{adh} (for the LEFM TDCB test specimen when using mild-steel or aluminium-alloy adherends)

4.4.2 Effect of the choice of adherend material

Figure 17a shows the variation of the adhesive fracture energy, G_a, as a function of the thickness of the adhesive layer, h_{adh}, as numerically predicted for the LEFM TDCB test, but now employing mild-steel adherends instead of aluminium-alloy adherends; and again with the crack propagating along the centreline of the adhesive layer. Figure 17a also shows the modelling results of Fig. 13a that were obtained for the TDCB test specimens with aluminium-alloy adherends. When using mild-steel adherends, the value of G_a is predicted to rise more slowly, and to reach a higher peak value, with the peak value now being about 20 J/m^2 higher and occurring at $h_{adh} \cong 0.6$ mm. After this peak value has been attained, the value of G_a again decreases in Regime III for the TDCB test specimen using the mild-steel adherends, but always remains consistently somewhat higher by about 20 J/m^2 compared with the values of G_a for the TDCB specimen employing the aluminium-alloy adherends.

Figure 17b shows that the constraint factor at the crack tip, f, is higher when the mild-steel adherends are employed for the TDCB test specimen. Although the effect is relatively small, this observation is valid regardless of the thickness of the adhesive layer, but is especially marked for h_{adh} values below 0.6 mm. The fundamental reasons for these predictions are that (a) the modulus of mild steel is approximately three times higher than that for the aluminium alloy (see Table 3), and (b) the adherend has a greater impact on the degree of constraint at the crack tip when h_{adh} is small. Now, it should be recalled that a higher degree of constraint leads to a lower extent of plastic-energy dissipation. Thus, these observations explain why, when the mild-steel adherend is used as opposed to the aluminium alloy, the values of Γ_b and, hence,

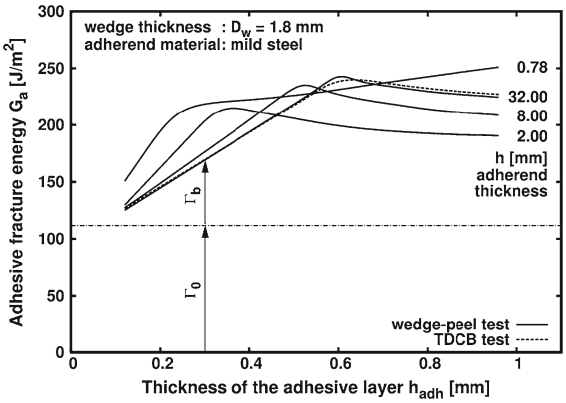

Fig. 18 The predicted adhesive fracture energy, G_a, as a function of the thickness of the adhesive layer, h_{adh}, for the EPFM wedge-peel test specimen, for different adherend thicknesses, h

the adhesive fracture energy, G_a, (a) increase more slowly in Regime II, and (b) attain a somewhat similar peak value but at a higher thickness of the adhesive layer.

4.5 Parametric modelling of the adhesive fracture energy, G_a, for the EPFM wedge-peel test

4.5.1 Effect of the thickness of the adhesive layer, h_{adh}

Figure 18 shows the numerically-predicted values of the adhesive fracture energy, G_a, as a function of the adhesive layer thickness, h_{adh}, for the EPFM wedge-peel test geometry using mild-steel adherends of different thicknesses, h, with the crack always running along the centreline of the adhesive layer. Figure 18 also shows the values of G_a, from Fig. 17a, that were predicted for the TDCB test, also employing mild-steel adherends. For the EPFM wedge-peel tests, with the exception of the results for an adherend thickness of 0.78 m, see below, all the predicted relationships follow a similar variation of G_a as a function of the thickness of the adhesive layer, h_{adh}, as was observed for the TDCB test. Namely, the value of G_a first increases linearly and then decreases, after reaching a peak, to a plateau value. The rationale for this behaviour arises from the reasons discussed in Sect. 4.4.1 for the LEFM TDCB specimens. That is, the values of Γ_b and, hence, G_a first increase with increasing h_{adh}, as there is more material available for plastic dissipation. They then decrease in value as the gradient of constraint from the crack plane to the adhesive/adherend interface decreases, which leads to plastic Zone C disappearing.

Considering the results for the EPFM wedge peel tests for an adherend thickness of 0.78 mm, then bending of the adhesive-coated adherend arms starts to become very significant when using such very thin arms for the adherends. The relatively large degree of bending that occurs induces extra stresses in the adhesive layer which, in turn, magnify the plastic dissipation in Zones A and B, since these are located where the bending stresses are the largest in the adhesive layer, see Fig. 10a. As the thickness of the adhesive layer is increased, the bending stresses become larger, since the adhesive layer increasingly contributes to the flexural stiffness of the arms. Hence, the plastic dissipation in Zones A and B steadily increases with increasing thickness of the adhesive layer, instead of reaching a plateau value. Thus, the G_a versus h_{adh} relationship corresponding to $h = 0.78$ mm does not show any peak, even though Zone C disappears, but the value of G_a keeps steadily increasing for thicker adhesive layers. Indeed, the wedge-peel test using arms of a thickness of 0.78 mm is predicted to give values of G_a higher by as much as 50 J/m^2 compared with the results from the other wedge-peel test configurations and with the numerically-predicted values for the TDCB test. However, as will be shown below in Sect. 4.5.4, when such bending effects are taken into account in the present model the results shown in Fig. 18 for the wedge-peel test employing an adherend thickness of 0.78 mm follow a similar trend to the other results shown in Fig. 18.

4.5.2 Effect of the thickness of the adherend, h

Ignoring, for the reasons discussed above, the results for the wedge-peel test employing adherend arms with a thickness of 0.78 mm, then Fig. 18 shows that, as the thickness of the arms, h, is increased, the value of G_a (a) rises more slowly as the thickness of the adhesive layer is increased, and (b) reaches a higher peak value, which occurs when the adhesive layer is somewhat thicker. This modification of the G_a versus h_{adh} relationship is similar to that associated with using a relatively high-modulus adherend material in the LEFM TDCB test, see Fig. 17a. These common observations arise since, in both types of test specimen, as the stiffness of the adherend is increased the constraint in the

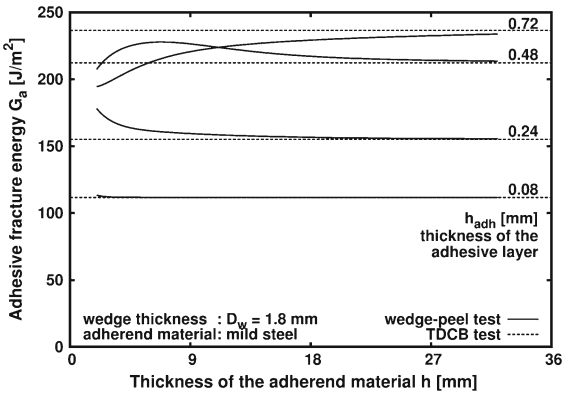

Fig. 19 The predicted adhesive fracture energy, G_a, as a function of the thickness of the adherend arms, h, for the different EPFM wedge-peel test configurations

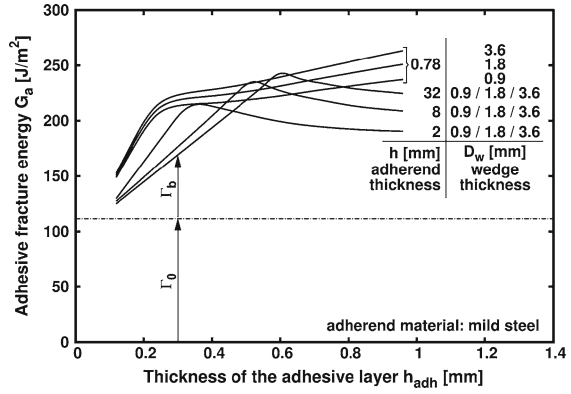

Fig. 20 The predicted values of the adhesive fracture energy, G_a, as a function of the thickness of the adhesive layer, h_{adh}, for the EPFM wedge-peel test specimen, for different test configurations with varying adherend, h, and wedge, D_w, thicknesses

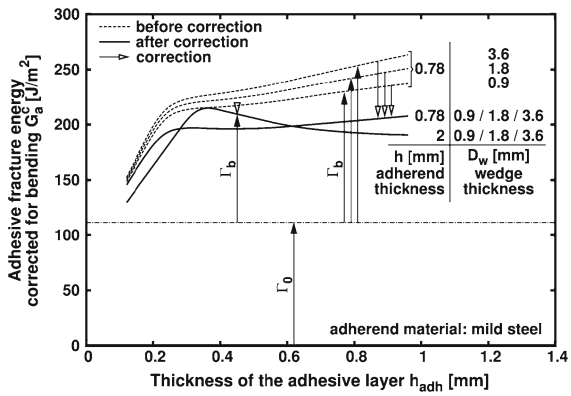

Fig. 21 The predicted adhesive fracture energy, G_a, corrected for bending in the adhesive layer, as a function of the thickness of the adhesive layer, h_{adh}, for different EPFM wedge-peel test configurations, with varying adherend, h, and wedge, D_w, thicknesses

adhesive becomes larger, which delays the development of plastic deformation to thicker adhesive layers. Figure 18 also shows (see the dashed line) that, as the thickness of adherend is increased, the G_a versus h_{adh} relationship for the EPFM wedge-peel tests is predicted to converge with that for the LEFM TDCB test. This feature is illustrated even more clearly in Fig. 19, which shows the values of G_a as a function of the adherend thickness, h, for different representative thicknesses of the adhesive layer, h_{adh}, predicted for the EPFM wedge-peel test. Figure 19 also shows that, depending on whether the thickness of the adhesive layer, h_{adh}, corresponds to before, or after, the peak value seen in G_a, the value of G_a predicted for the wedge-peel test decreases, or increases, by a maximum of about 30 J/m^2 as the value of h is changed, before finally attaining the LEFM TDCB value at an adherend thickness, h, of about 20 mm.

4.5.3 Effect of the thickness of the wedge, D_w

Figure 20 shows the effect of the thickness of the wedge, D_w, on the G_a versus h_{adh} relationship for the wedge-peel test. Significant effects of the wedge thickness are only observed for specimens where a major contribution from the bending in the adhesive occurs, i.e. for an adherend thickness, $h = 0.78$ mm. Here a thicker wedge induces more bending in the adhesive-coated adherends. This magnifies the associated plastic-energy dissipation in the adhesive layer, and so induces an increase in the value of the adhesive fracture energy, G_a, in proportion to the initial amount of bending.

4.5.4 Adhesive bending corrections

Figure 21 shows the values of G_a corresponding to $h = 0.78$ mm and $h = 2$ mm, from Fig. 20, before and after a correction has been applied for the extra plastic-energy dissipated in the adhesive layer as a result of any bending of the adhesive-coated adherend arms. This correction was evaluated numerically, as an approximation,[5], as the energy expended in the adhesive should

[5] The adhesive behaves plastically and, hence, non-linearly at crack tip so that the principle of superposition does not apply. The total energy cannot therefore rigorously be evaluated as the sum of the energy expended in bending in the absence of a crack tip and at the crack tip in the absence of bending.

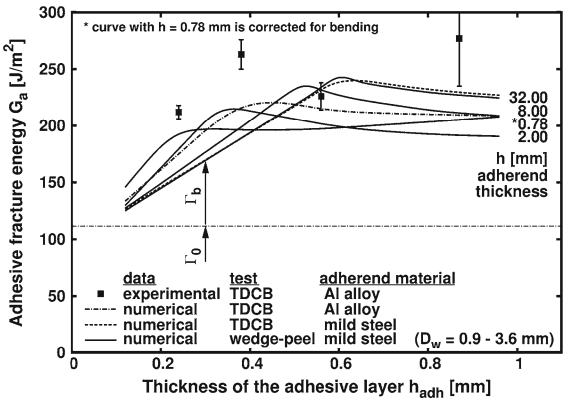

Fig. 22 The predicted adhesive fracture energy, G_a, as a function of the thickness of the adhesive layer, h_{adh}, for the different test specimens and test configurations; and compared with the experimental values obtained from the LEFM TDCB test specimens using aluminium-alloy adherends

the specimens be cut along the crack plane prior to being forced to follow the exact same deformation of the arms as seen in the wedge-peel test. As discussed in Sect. 4.5.1, the correction is insignificant for adherend arms with a thicknesses of 2 mm, and above, and is only significant for values of $h = 0.78$ mm. Further, Fig. 21 reveals that, after correcting for this extra plastic-energy dissipation associated with bending in the adhesive layer for the wedge-peel test with $h = 0.78$ mm, then firstly the effect of the wedge thickness, D_w, vanishes. Secondly, the adhesive fracture energy, G_a, as a function of the thickness of the adhesive layer, h_{adh}, relationship for the $h = 0.78$ mm wedge-peel test is now in good agreement with the behaviour predicted for such tests with thicker adherend arms.

4.6 Concluding comments on the constraint effects and generalization of the model

Figure 22 shows the numerically-predicted values of the adhesive fracture energy, G_a, as a function of the adhesive layer thickness, h_{adh}, for the LEFM TDCB and EPFM wedge-peel test configurations discussed in Sects. 4.4 and 4.5 (for the wedge-peel test specimen with adherend arms of $h = 0.78$ mm, the values have been corrected for bending, as discussed above). Figure 22 also includes the G_a values that were obtained experimentally from the TDCB test specimens using aluminium-alloy adherends, which failed close to the centreline of the adhesive layer; see also Fig. 8b and Table 2. Several noteworthy points arise. Firstly, there is an extensive body of literature which establishes the dependence of G_a, as a function of h_{adh}, see for example Kinloch (1987). The same trends are, as expected, seen in the present work both from (a) the experimental studies, see Fig. 8a, b and Table 2, and (b) the predicted modelling studies, see Figs. 8a, b, 13a, 17a, 18, 20, 21 and 22. Secondly, as commented previously, for the TDCB test, the numerical values of G_a predict quite well the variation of G_a with h_{adh}, that was observed experimentally, namely a steady increase up to a plateau value after passing through a small local peak at an intermediate thickness of $h_{adh} \cong 0.40$ mm. Thirdly, from Fig. 22, all the numerically-predicted values of G_a, for a given value of h_{adh}, vary by only about ± 20 J/m^2 (i.e. a coefficient of variation of about $\pm 10\%$) for the two types of test specimen and the various test configurations. Fourthly, Fig. 22 reveals that this variation is of the same order of magnitude as the scatter measured when determining the values of G_a experimentally. Therefore, fifthly, the modelling studies predict no statistically significant differences will be observed in the experimentally-measured G_a values, for a given value of the thickness of the adhesive layer, h_{adh}, associated with the different test specimens and other aspects of the test configurations.

The above conclusions support the hypothesis of considering the measured value of the adhesive fracture energy, G_a, as a 'characteristic material property' of the adhesive joint, for a given thickness of the adhesive layer h_{adh}. Indeed, the independence of the value of G_a upon the type of test specimen, or upon the choice of adherend material, when the locus of joint is cohesive through the adhesive layer, has been previously observed experimentally for a relatively tough adhesive by Blackman et al. (2003c) and by Kawashita et al. (2008). Further, Martiny et al. (2008), following a modelling approach very similar to the present one, were able to predict numerically the independence of the adhesive fracture energy upon the test specimen and test configuration for this adhesive, for a given thickness of the adhesive layer. In this case, this theoretical confirmation of the previous experimental results arose from the energy expenditure in the bulk of the adhesive layer, i.e. the Γ_b term in Eq. (18), being negligible. Hence, the value of G_a was approximately equal to the constant value of the intrinsic fracture energy, Γ_0, regardless of the details of the test specimen or test configuration. In contrast, in the present study using the

relatively low toughness adhesive, it may be seen from Fig. 22 that the Γ_b term does now contribute significantly, i.e. up to 50%, to the value of G_a. Nevertheless, the values of G_a, at a given value of h_{adh}, are still relatively independent of the test details; and this finding arises from the value of Γ_b being relatively independent of the exact details of the test specimen, or other aspects of the test configuration which do not significantly affect the constraint.

The understanding gained in the present work can be transferred to other systems if two conditions are met. First, as explained above, all the variations of the different dissipative terms with thickness will be important only if the term Γ_b is a significant fraction of the intrinsic fracture energy, Γ_0. This is true in the system studied here due to the intrinsically low toughness combined to a sufficiently high peak stress, large enough to generate enough plastic dissipation. This is why we have insisted on the "low toughness" characteristics of the present system. The possible contribution of the plastic dissipation to the toughness can be assessed by performing tests on different adhesive thicknesses. Second, the relevance of the conclusions reached in this study rely on the assumption of a constraint independent constant Γ_0. For the present adhesive, this hypothesis is indirectly verified by the good agreement between the simulation results and the experimental data. Although the micromechanical analysis of the failure mechanisms is outside the scope of the present paper, it is known, as observed in earlier investigations (Ferracin 2003), that the damage mechanism in the present adhesive involves the fracture of the silicate particles. This relatively brittle mechanism does probably not depend much on the level of stress triaxiality. We anticipate that a damage mechanism involving the growth of voids inside the fracture process zone will be much more dependent on the stress triaxiality level, and will require a constraint dependent Γ_0 as already discussed in the literature in the context of ductile failure of metals, e.g. Tvergaard and Hutchinson (1996), Siegmund and Brocks (1998), Pardoen et al. (1999), and recently by McAuliffe et al. (2011) for adhesive bonds.

5 Conclusions

The numerical model developed in the present study for a typical low-toughness epoxy-based structural adhesive has been shown, by comparison with experimental data, to be capable of reproducing accurately the failure of different types, and geometrical configurations, of adhesive joints employing a single set of material parameters in the cohesive zone model. It has further been shown to be well suited to studying efficiently, for the same adhesive, many extra design configurations in the framework of a parametric study. More particularly, numerical-modelling studies have been successfully undertaken to predict how the type of test specimen and test configuration (e.g. the thickness of the adhesive layer, and the thickness and type of adherend material) affect the value of the adhesive fracture energy, G_a. Furthermore, the different sources of energy dissipation in the bulk of the adhesive layer which contribute to the value of G_a have been identified and quantified for each design configuration which has been simulated numerically.

The detailed modelling studies undertaken in the present paper have highlighted several fundamental conclusions which are given below. These results, though directly pertaining to the particular adhesive studied here, are considered to be of a general qualitative nature and should undoubtedly form a firm basis for the study and the understanding of the fracture of other structural adhesives. The most noteworthy of such conclusions are:

- Some elastic energy is generally locked-in the adhesive when it is fractured, but the main contributions to the adhesive fracture energy, G_a, come from (a) the localised damage and deformation mechanisms immediately ahead of the crack tip called the 'fracture process zone' and associated with the intrinsic work of fracture, Γ_0, and (b) the plastic-energy dissipation in the bulk adhesive layer.
- Three zones of plastic dissipation generally develop in the bulk adhesive layer, each of them involving a distinct mechanism: crack tip plasticity, reverse plastic loading and plastic shear deformation at the adhesive/adherend interface. The magnitude of the crack tip plasticity increases with a decreasing degree of constraint at the crack tip. The contribution of the reverse plasticity has in most cases a second-order effect on the value of the adhesive fracture energy, G_a. The extent of plastic shear deformation at the adhesive/adherend interface increases with the gradient of constraint between the crack plane and the adhesive/adherend interface. These three sources of plastic dissipation

are all magnified by any bending stresses that may be present in the adhesive layer, e.g. during a peel test.

- The adhesive fracture energy, G_a, is indeed a strong nonlinear function of the thickness of the adhesive layer, as observed experimentally by many researchers. For the present adhesive, the value of G_a ranges between 120 and 250 J/m^2 for bondline thicknesses in the range of 0.1–1.0 mm. As the thickness of the adhesive layer is increased, the adhesive fracture energy first increases, since there is more adhesive material available for plastic dissipation and because the degree of constraint at the crack tip decreases. The value of G_a then decreases after passing through a peak as the plastic zone associated with the plastic shear deformation at the adhesive/adherend interface vanishes, since the gradient of constraint between the crack plane and the interface now decreases dramatically.
- The value of the adhesive fracture energy may also strongly depend upon the locus of failure. This may basically be cohesive in nature, but actually be via either a cohesive failure near the centreline of the adhesive layer or a cohesive failure near one of the adhesive/adherend interfaces. This effect is considered to share common features with the effect of the thickness of the adhesive layer, since the locus of failure actually modifies the distance between the crack plane and the adhesive/adherend interfaces.
- When using relatively thick and/or high-modulus adherends, the details of the adherends (e.g. thickness and material type) and the type of test are of secondary importance on the value of the adhesive fracture energy, G_a. This prediction from the modelling studies is in agreement with several experimental studies to be found in the literature. For the present adhesive, changing such parameters generally modified the value of G_a by no more than $\pm 10\%$. These minor effects may all be explained by the higher degree of constraint that is imposed by employing thicker and/or stiffer adherends.
- When employing sufficiently thin adherends, the adhesive layer significantly contributes to the bending stiffness of the bonded joint. As a result, significant bending stresses develop in the adhesive. These may magnify the different sources of plastic energy dissipation.
- Finally, the modelling results for the present relatively low-toughness adhesive strongly support the hypothesis of the adhesive fracture energy, G_a, being a 'characteristic material property' of the adhesive joint, for a given thickness of the adhesive layer h_{adh}, which is independent of the test specimen and other aspects of the test configuration. This conclusion arises not from the value of Γ_b being negligible, as found in previous work of Martiny et al. (2008) for a different, relatively high-toughness adhesive, which possessed a G_a value of about 1,000 J/m^2. In contrast, in the present studies, this conclusion arises from the value of Γ_b being almost independent of the exact details of the test specimen or test configuration, apart of course from being dependent on the value of the thickness of the adhesive layer, h_{adh}. Indeed, the numerically-predicted values of G_a, at a given value of h_{adh}, vary by only about ± 20 J/m^2, i.e. a coefficient of variation of about $\pm 10\%$, for the many different types of test specimen and the various test configurations; and this is well within the precision of the experimentally-measured values of G_a from such tests.

Acknowledgments The present work was carried out under the SINUS project, jointly funded by the Walloon Region (Belgium) and the European ERDF. The authors are grateful to Dr. F. S. Rodriguez Sanchez (Imperial College London) and Mr. B. Wucher (École Centrale de Nantes) for their experimental and computational assistance.

References

Bascom WD, Cottington RL, Jones RL, Peyser P (1975) The fracture of epoxy- and elastomer-modified epoxy polymers in bulk and as adhesives. J Appl Polym Sci 19:2545–2562

Blackman BRK, Hadavinia H, Kinloch AJ, Paraschi M, Williams JG (2003a) The calculation of adhesive fracture energies in mode I: revisiting the tapered double cantilever beam (TDCB) test. Eng Fract Mech 70:233–248

Blackman BRK, Hadavinia H, Kinloch AJ, Williams JG (2003b) The use of a cohesive zone model to study the fracture of fibre composites and adhesively-bonded joints. Int J Fract 119:25–46

Blackman BRK, Kinloch AJ, Paraschi M, Teo WS (2003c) Measuring the mode I adhesive fracture energy, G_{IC}, of structural adhesive joints: the results of an international round-robin. Int J Adhes Adhes 23:293–305

Chai H (1986) Bond thickness effect in adhesive joints and its significance for mode I interlaminar fracture of composites. In: Composite materials testing and design, ASTM-STP 893, pp 209–231

Chai H (1988) Fracture work of thin bondline adhesive joints. J Mater Sci Lett 7:399–401

Chai H, Chiang MYM (1998) Finite element analysis of interfacial crack propagation based on local shear, Part II—fracture. Int J Solids Struct 35:815–829

Cooper V, Ivankovic A, Karac A, Murphy N (2009) The effect of constraint on the fracture toughness of adhesively bonded joints. In: Proceedings of the 32nd annual meeting of the Adhesion Society, Savannah, pp 33–35

Cui J, Wang R, Sinclair AN, Spelt JK (2003) A calibrated finite element model of adhesive peeling. Int J Adhes Adhes 23: 199–206

Dean RH, Hutchinson JW (1980) Quasi-static steady crack growth in small-scale yielding. In: Fracture mechanics, ASTM-STP 700, pp 383–405

Drugan WJ, Rice JR, Sham TL (1982) Asymptotic analysis of growing plane strain tensile cracks in elastic-ideally plastic solids. J Mech Phys Solids 30:447–473

Ferracin T (2003) Mechanics of failure in adhesively bonded steel assemblies. PhD Thesis, Université catholique de Louvain, Belgium

Ferracin T, Landis CM, Delannay F, Pardoen T (2003) On the determination of the cohesive zone properties of an adhesive layer from the analysis of the wedge-peel test. Int J Solids Struct 40:2889–2904

Hadavinia H, Kawashita L, Kinloch AJ, Moore DR, Williams JG (2006) A numerical analysis of the elastic-plastic peel test. Eng Fract Mech 73:2324–2335

Hunston DL, Kinloch AJ, Wang SS (1989) Micromechanics of fracture in structural adhesive bonds. J. Adhes. 28:103–114

Hutchinson JW, Evans AG (2000) Mechanics of materials: top-down approaches to fracture. Acta Mater 48:125–135

Kafkalidis MS, Thouless MD, Yang QD, Ward SM (2000) Deformation and fracture of adhesive layers constrained by plastically-deforming adherends. J Adhes Sci Technol 14:1593–1607

Kawashita LF, Moore DR, Williams JG (2008) The influence of bond line thickness and peel arm thickness on adhesive fracture toughness of rubber toughened epoxy-aluminium alloy laminates. Int J Adhes Adhes 28:199–210

Kinloch AJ (1987) Adhesion and adhesives: science and technology, 1st edn. Chapman & Hall, London

Kinloch AJ, Shaw SJ (1981) The fracture resistance of a toughened epoxy adhesive. J Adhes 12:59–77

Landis CM, Pardoen T, Hutchinson JW (2000) Crack velocity dependent toughness in rate dependent materials. Mech Mater 32:663–678

Martiny Ph, Lani F, Kinloch AJ, Pardoen T (2008) Numerical analysis of the energy contributions in peel tests: a steady-state multilevel finite element approach. Int J Adhes Adhes 28:222–236

McAuliffe D, Karac A, Murphy N, Ivankovic A (2011) Transferability of adhesive fracture toughness measurements between peel and TDCB test methods for a nano-toughened epoxy. In: Proceedings of the 34th annual meeting of the Adhesion Society, Savannah (USA)

Minamo (2010) Web page: http://www.cenaero.be/Minamo

Needleman A (1987) A continuum model for void nucleation by inclusion debonding. J Appl Mech 54:525–531

Pardoen T, Marchal Y, Delannay F (1999) Thickness dependence of cracking resistance in thin aluminium plates. J Mech Phys Solids 47:2093–2123

Pardoen T, Ferracin T, Landis CM, Delannay F (2005) Constraint effects in adhesive joint fracture. J Mech Phys Solids 53:1951–1983

Rice JR (1967) Fatigue crack propagation. In: Fatigue crack propagation, ASTM-STP 415, p 247

Salomonsson K, Andersson T (2008) Modeling and parameter calibration of an adhesive layer at the meso level. Mech Mater 40:48–65

Siegmund T, Brocks W (1998) Local fracture criteria: length-scales and applications. In: Proceedings of the 2nd Euromech-Mecamat conference, Magdeburg, pp 347–354

Tvergaard V (1990) Effect of fiber debonding in a whisker-reinforced metal. Mater Sci Eng A 125:203–213

Tvergaard V, Hutchinson JW (1992) The relation between crack growth resistance and fracture process parameters in elastic-plastic solids. J Mech Phys Solids 40:1377–1397

Tvergaard V, Hutchinson JW (1994) Toughness of an interface along a thin ductile layer joining elastic solids. Phil Mag A 70:641–656

Tvergaard V, Hutchinson JW (1996) Effect of strain-dependent cohesive zone model on predictions of crack growth resistance. Int J Solids Struct 33:3297–3308

Wei Y, Hutchinson JW (1997) Nonlinear delamination mechanics for thin films. J Mech Phys Solids 45:1137–1159

Yang QD, Thouless MD, Ward SM (1999) Numerical simulations of adhesively-bonded beams failing with extensive plastic deformation. J Mech Phys Solids 47:1337–1353

Yang QD, Thouless MD, Ward SM (2000) Analysis of the symmetrical 90°-peel test with extensive plastic deformation. J Adhes 72:115–132